

Scaling of pressure fluctuations in compressible turbulent plane channel flow

G.A. Gerolymos¹ and I. Vallet^{1,†}

¹Faculty of Engineering, Sorbonne Université, 4 place Jussieu, 75005 Paris, France

(Received 1 July 2022; revised 14 November 2022; accepted 9 January 2023)

The purpose of the paper is to identify Mach-number effects on pressure fluctuations p' in compressible turbulent plane channel flow. We use data from a specifically constructed $(Re_{\tau^*}, \bar{M}_{CL_x})$ -matrix direct numerical simulation (DNS) database, with systematic variation of the centreline streamwise Mach number $0.32 \leq \bar{M}_{CL_x} \leq 2.49$ and of the HCB (Huang *et al.*, *J. Fluid Mech.*, vol. 305, 1995, pp. 185–218) friction Reynolds number $66 \leq Re_{\tau^*} \lesssim 1000$. Strong \bar{M}_{CL_x} effects (enhanced by the increasingly cold-wall condition) appear for $\bar{M}_{CL_x} \gtrsim 2$, for all Re_{τ^*} , very close to the wall ($y^* \lesssim 15$). Compared with incompressible flow at the same Re_{τ^*} , the wall root-mean-square $[p'_{rms}]_w^+$ (in wall-units, i.e. scaled by the average wall shear stress $\bar{\tau}_w$) strongly increases with \bar{M}_{CL_x} . In contrast, the peak level across the channel, $[p'_{rms}]_{PEAK}^+$, slightly decreases with increasing \bar{M}_{CL_x} . In order to study the near-wall coherent structures we introduce a new wall-distance-independent non-local system of units, based for all y on wall friction and the extreme values of density and dynamic viscosity, namely, for cold walls $\{\bar{\tau}_w, \min_y \bar{\rho}, \max_y \bar{\mu}\}$. The average spanwise distance between streaks, scaled by this length-unit, is nearly independent of \bar{M}_{CL_x} at constant Re_{τ^*} . Using the in-plane (parallel to the wall) Laplacian $\nabla_{xz}^2 p'$ we find that the $(+/-)-p'$ wave-packet-like structures appearing inside the low-speed streaks ($y^* \lesssim 15$) with increasing $\bar{M}_{CL_x} \gtrsim 2$ are part of a more complex wave system with spanwise extent over several streaks, whose spatial density decreases rapidly with decreasing \bar{M}_{CL_x} or increasing y^* . These p' wave packets appear to be collocated with strong $(+/-)-v'$ events and could be responsible for compensating towards 0 the negative incompressible-flow correlation coefficient $c_{p'v'}$, with increasing \bar{M}_{CL_x} very near the wall.

Key words: turbulent boundary layers, compressible boundary layers, turbulence theory

† Email address for correspondence: isabelle.vallet@sorbonne-universite.fr

1. Introduction

Substantial effort has been devoted to the study of pressure fluctuations in incompressible wall turbulence using theoretical approaches (Panton & Linebarger 1974), direct numerical simulation (DNS) (Kim 1989) and experiments in wind tunnels (Tsuji *et al.* 2007) or in the atmospheric boundary-layer (Klewicki, Priyadarshana & Metzger 2008). DNS is still limited in the high-Reynolds-number range by available computer resources, the highest reported friction Reynolds number being $Re_{\tau_w} = 10\,045$ (Hoyas *et al.* 2022), whereas experiments are confronted with the difficult problem of filtering out parasite wind-tunnel noise (Tsuji *et al.* 2012) and the frequency response of the transducers (Tsuji *et al.* 2007). Regarding the scaling of the wall fluctuation level $(p'p')_w^+$ in incompressible flow, Panton, Lee & Moser (2017) used inner/outer matched asymptotic expansions to justify $(\ln Re_{\tau_w})$ -scaling which suggests unbounded growth of inner-scaled $[p'_{rms}]_w^+$ with Re_{τ_w} , but a finite limit when using mixed scaling $\rho u_\tau \bar{u}_{CL} = \bar{\tau}_w \sqrt{2/c_f}$ for p' instead. However, recent work by Chen & Sreenivasan (2022) argues that a $Re_{\tau_w}^{-1/4}$ -scaling (yielding a finite limit in wall-units as $Re_{\tau_w} \rightarrow \infty$) is more consistent with data, in line with the matched asymptotic analysis of Monkewitz (2022) for the streamwise velocity covariance $\overline{u^2}$. Standard notation (Smits & Dussauge 2006, pp. 61–65), $(\cdot) = (\bar{\cdot}) + (\cdot)' = (\tilde{\cdot}) + (\cdot)''$, for Reynolds or Favre averages and fluctuations, is used throughout the paper.

Incompressible flow data, both for channels (Lee & Moser 2015) and zero-pressure-gradient (ZPG) boundary layers (Schlatter *et al.* 2010), reveal (Panton *et al.* 2017) a reasonably robust inner law (near-wall behaviour) for the $p'_{rms}(y^+)$ profiles, with a peak (local maximum) $[p'_{rms}]_{PEAK}^+$ around $28 \lesssim y_{PEAK}^+ \lesssim 32$ (depending on Re_{τ_w}), and a lower level $[p'_{rms}]_w^+$ at the wall (p'_{rms} is nearly constant very near the wall, for $y^+ \lesssim 5$). It is believed (Kim & Hussain 1993) that very near the wall ($y^+ \lesssim 5$) turbulent perturbations essentially propagate with y -independent velocity, and frozen-wave estimates (del Álamo & Jiménez 2009) in compressible turbulent boundary layers (TBLs) (Zhang, Duan & Choudhari 2017) suggest that this is also the case in compressible wall turbulence.

The detailed investigation by Bernardini & Pirozzoli (2011) of $2 \leq M_\infty \leq 4$ ZPG TBLs over an adiabatic wall (more precisely an isothermal wall at the adiabatic-wall recovery temperature $T_w = T_r$) does not indicate substantial changes in the near-wall $p'_{rms}(y^+)$ profiles. Nonetheless, careful examination of the data indicates that small changes do occur, both $[p'_{rms}]_w^+$ and $[p'_{rms}]_{PEAK}^+$ slightly increasing with \bar{M}_{δ_x} . This very-near-wall behaviour is also observed in compressible turbulent plane channel (TPC) flow, already at much lower \bar{M}_{CL_x} (Gerolymos & Vallet 2014; Modesti & Pirozzoli 2016; Tang *et al.* 2020). At $(Re_{\tau^+}, \bar{M}_{CL_x}) = (113, 2.49)$, $[p'_{rms}]_w^+$ is already higher than $[p'_{rms}]_{PEAK}^+$ (Gerolymos & Vallet 2014; Tang *et al.* 2020). In contrary to adiabatic-wall ZPG TBL studies (Bernardini & Pirozzoli 2011) the wall is increasingly colder with increasing \bar{M}_{CL_x} in TPC flows (Coleman, Kim & Moser 1995; Gerolymos & Vallet 2014), resulting in lower sound-speed near the wall compared with the centreline, and consequently to higher \bar{M}_x/\bar{M}_{CL_x} near the wall compared with adiabatic-wall ZPG TBLs. This effect of wall temperature was demonstrated by Zhang *et al.* (2017) who studied the effect of $\bar{T}_w/T_r \in \{1, 0.76, 0.25\}$ in a $M_\infty = 5.86$ ZPG TBL. As \bar{T}_w/T_r decreases (colder wall) the wall-to-peak ratio $[p'_{rms}]_w/[p'_{rms}]_{PEAK}$ increases to reach $\sim \frac{3}{2}$ at $\bar{T}_w/T_r = 0.25$ (Zhang *et al.* 2017). The major influence of \bar{T}_w/T_r at constant \bar{M}_{CL_x} has also been demonstrated for TPC flow by Yu & Xu (2021) who added an artificial sink term (cooling) in the energy equation (Yu, Xu &

Pirozzoli 2020), thus controlling the ratio \bar{T}_w/T_r , following the approach used by Coleman *et al.* (1995) to create an equivalent artificial flow without temperature stratification.

These important changes of the $p'_{rms}(y)$ profiles very near the wall, with increasing Mach number (\bar{M}_{CL_x} or \bar{M}_{δ_x}) and/or decreasing \bar{T}_w/T_r (colder wall) are obviously the footprint of changes in the very-near-wall turbulence structure. Coleman *et al.* (1995) who were the first to study the canonical compressible TPC flow, observed increased streamwise coherence of the near-wall streaks with increasing \bar{M}_{CL_x} , inducing increased mean shear $\partial_y \bar{u}$ because of stronger $\{\rho, T\}$ -stratification of the near-wall region (demonstrated by simulating an artificial flow without the viscous heating term $\overline{\tau_{ij} S_{ij}}$ in the static temperature equation thus recovering the incompressible flow spanwise coherence and changing the near-wall sign of correlation coefficient $c_{\rho'T'} < 0$ back to $c_{\rho'T'} > 0$). They also discussed the possibility to consider the (high/low)-speed regions of the near-wall flow as ‘variable density mixing layer(s) at the edge of a cold low-speed streak ... governed by the same dynamics responsible for the reduced spreading rate of compressible mixing layers (Papamoschou & Roshko 1988) ... for convective Mach number $M_c > 0.5$ ’. Coleman *et al.* (1995) considered that observed M_c were too weak to induce such compressibility effects, without however detailing how M_c is defined with respect to the observed coherent structures and the wall proximity.

Tang *et al.* (2020) compared two TPC flows, at $(Re_{\tau^*}, \bar{M}_{CL_x}) \in \{(110, 2.39), (340, 1.50)\}$, to investigate compressibility effects on p' . Following Sarkar (1992) they used the compressible Poisson equation for p' (Sarkar 1992; Foysi, Sarkar & Friedrich 2004; Gerolymos, Sénéchal & Vallet 2013) to split $p' = p'_{(r)} + p'_{(s)} + p'_{(\tau)inc} + p'_{(c)}$ into slow ($p'_{(s)}$), rapid ($p'_{(r)}$), incompressible Stokes ($p'_{(\tau)inc}$) and the remainder identified as the compressible contribution $p'_{(c)}$ (Sarkar 1992). In compressible flow the source term for the Stokes term $Q'_{(\tau)} \neq 0$ (Foysi *et al.* 2004; Gerolymos *et al.* 2013), in contrast to the calculated $p'_{(\tau)inc}$. There was therefore a part of Stokes $p'_{(\tau)}$ included in the compressible $p'_{(c)}$. The instantaneous p' -fields revealed fundamental changes between the $\bar{M}_{CL_x} = 1.50$ case and the higher $\bar{M}_{CL_x} = 2.39$ flow, with the appearance at $\bar{M}_{CL_x} = 2.39$ of alternating $(+/-)$ - p' structures, essentially located inside the low-speed streaks. These $(+/-)$ - p' structures were further identified (Tang *et al.* 2020) in linearised mode analyses, were associated to the observed differences (with increasing \bar{M}_{CL_x}) in wavenumber and frequency spectra, and were shown to be the result of the compressible mechanism $p'_{(c)}$ which increased substantially compared with the other mechanisms (Tang *et al.* 2020). These $(+/-)$ - p' structures are related with the significant dilatational perturbations focused along the cold slow-sound-velocity low-speed streaks possibly acting as acoustic waveguides (Coleman *et al.* 1995).

Yu, Xu & Pirozzoli (2019) opted for the kinematic decomposition of the velocity field $u_i = u_{\omega_i} + u_{\Theta_i}$, into a solenoidal part induced by the instantaneous vorticity distribution $\omega_i := \epsilon_{ijk} \partial_{x_j} u_k$ and an irrotational part induced by the instantaneous dilatation distribution $\Theta := \partial_{x_k} u_k$ (Batchelor 1967, pp. 84–87), to study the effects of $0 < \bar{M}_{CL_x} \leq 6.97$ (including an incompressible DNS) and of the wall-to-recovery temperature ratio \bar{T}_w/T_r , where T_r is the adiabatic wall recovery temperature (van Driest 1951). The ratio \bar{T}_w/T_r was adjusted (Yu *et al.* 2019) by an artificial sink term (cooling) in the energy equation, in line with the study on temperature stratification effects in Coleman *et al.* (1995). Instantaneous X-rays, at $y^+ = 15$, of the fluctuating velocity fields, at

$(\bar{M}_{CL_x}, Re_{\tau_w}, \bar{T}_w/T_r) \approx (3.48, 494, 0.5)$, revealed the presence of alternating $(+/-)-u''_{\ominus}$ patterns along the near-wall streaks, ‘probably interpretable as traveling wave packets’ (Yu *et al.* 2019). Yu *et al.* (2020) combined the $p' = p'_{(r)} + p'_{(s)} + p'_{(\tau)} + p'_{(c)}$ splitting (using the compressible $Q'_{(\tau)} \neq 0$) with the $u_i = u_{\omega_i} + u_{\ominus_i}$ splitting of the velocity field, showing that the increase in p'_{rms} near the wall is associated with similar increases in $[p'_{(c)}]_{rms}$ and $[p'_{(\tau)}]_{rms}$, whereas the rapid $[p'_{(r)}]_{rms}$ and slow $[p'_{(s)}]_{rms}$ profiles remained practically unaffected by compressibility effects.

These studies (Tang *et al.* 2020; Yu *et al.* 2019, 2020; Yu & Xu 2021) clearly correlate the modification, under the synergetic effect of increasing \bar{M}_{CL_x} (\bar{M}_{δ_x}) and decreasing \bar{T}_w/T_r , of the near-wall p'_{rms} profile, to the increase of $p'_{(c)}$. Another indication of the inception of compressibility effects in the near-wall region is the breakdown (or rather the increasing approximation error) of the linear approximations of thermodynamic correlations obtained by truncating the exact expressions implied by the fluctuating equation-of-state (EoS) (Gerolymos & Vallet 2018).

In previous work (Gerolymos & Vallet 2014, 2018) the simultaneous variation of both $(Re_{\tau^*}, \bar{M}_{CL_x})$ in the database hindered the unambiguous identification of the effect of each parameter. For this reason we constructed a $(Re_{\tau^*}, \bar{M}_{CL_x})$ -matrix database. The other important parameter in wall turbulence, namely \bar{T}_w/T_r , is not controlled in the present simulations of canonical compressible TPC flow (Coleman *et al.* 1995), but depends on $(Re_{\tau^*}, \bar{M}_{CL_x})$, because there is no artificial source term in the energy equation. The wall gets increasingly colder with increasing \bar{M}_{CL_x} . Although closer-to-adiabatic wall-temperature conditions are relevant in practical high-Mach-number applications (Zhang *et al.* 2017) TPC flow data are particularly useful for the study of thermodynamic turbulence structure (Gerolymos & Vallet 2018) and the transport of thermodynamic quantities in the inner layer (Gerolymos & Vallet 2014) including temperature (Bowersox 2009), especially as the exact streamwise invariance of the flow allows, via streamwise averaging, for much larger statistical samples in a given observation time.

The purpose of the paper is to study the effects of $(Re_{\tau^*}, \bar{M}_{CL_x})$ on the fluctuating pressure field p' , and to identify similarities and differences with incompressible flow data. We use the term compressible in a generic sense, making no distinction between mean flow stratification effects (Morkovin 1962) or compressible turbulence effects directly related to the fluctuating density ρ' (Gerolymos & Vallet 2014, 2018) either via the compressible terms in the Poisson equation for fluctuating pressure p' (Pantano & Sarkar 2002; Foyi *et al.* 2004; Tang *et al.* 2020) or identified in relation to the dilatation-induced velocity (Yu *et al.* 2019). In § 2, we briefly describe the construction of the database, summarize available data and introduce the three systems of units (defining the non-dimensionalisation scales) used in the paper. In § 3, we study the root-mean-square (r.m.s.) level of the fluctuating pressure, $p'_{rms} := \sqrt{\overline{(p'p')}}$ and pressure–velocity correlation coefficient $\{c_{p'u'}, c_{p'v'}\}$, clearly identifying the near-wall region (roughly $y^* \lesssim 15$) as the principal location of strong $(\bar{M}_{CL_x} \gtrsim 2)$ effects. We also determine an empirical correlation highlighting the dependence of $[p'_{rms}]_w$ on the three parameters $(Re_{\tau^*}, \bar{M}_{CL_x}, T_r/\bar{T}_w)$. In § 4, we investigate coherent structures in the near-wall region, focussing first (§ 4.1) on the \bar{M}_{CL_x} -scaling of the average spanwise distance between streaks (more precisely of its surrogate defined by the spanwise correlations of the streamwise velocity), leading to the choice of the appropriate non-dimensionalisation.

These new length-units correct the deficiency of HCB-length-units near the wall and are nearly identical to HCB-length-units further away from the wall. In § 4.2, we use the in-plane Laplacian $\nabla_{xz}^2 p'$ to identify (+/-)- p' fronts ($\nabla_{xz}^2 p' = 0$) and in § 4.3, we discuss the collocation of these fronts with the extrema of wall-normal velocity fluctuation v' (or, equivalently, of wall-normal Mach number $M'_y := (v/a)'$) and the structural modifications observed, with increasing \bar{M}_{CL_x} , in the joint probability density functions (p.d.f.s) of p' versus the fluctuating velocity components u'_i (which explain the very strong near-wall \bar{M}_{CL_x} effect on the correlation coefficient $c_{p'v'}$). Finally, in § 5, we present the conclusions of the present work and discuss directions for future research.

2. ($Re_{\tau^*}, \bar{M}_{CL_x}$)-scalings and database

Compressible TPC flow between two isothermal walls (Coleman *et al.* 1995) is characterised by mean temperature stratification, which strongly increases with increasing Mach number (figure 1), because of viscous heating $\overline{S_{ij}\tau_{ij}}$, especially near the wall (Coleman *et al.* 1995). Mean pressure $\bar{p}(y) = \bar{p}_w - \overline{\rho v''v''}$ (under the condition of streamwise invariance in the mean of plane compressible turbulent channel flow) varies little across the channel (increasingly so with increasing \bar{M}_{CL_x} , but never exceeding 3%; figure 1). Therefore, because of the perfect gas EoS $p = \rho R_g T \implies \bar{p} = \bar{\rho} R_g \bar{T}$, density $\bar{\rho}(y)$ varies almost inversely proportionally to temperature $\bar{T}(y)$. Finally, dynamic viscosity $\bar{\mu}(y)$, being a function of temperature (Gerolymos & Vallet 2014, (2.1), p. 706), varies in the same way as $\bar{T}(y)$ but with a lower exponent (figure 1).

2.1. Wall-units and mixed scalings

Because of this $\{\bar{\rho}, \bar{T}, \bar{\mu}\}$ -stratification (figure 1), Huang, Coleman & Bradshaw (1995) realised that the standard wall-units inherited by incompressible flow analyses

$$(\cdot)^+ \text{ units: } \{\bar{\tau}_w, \bar{\mu}_w, \bar{\rho}_w\} \implies y^+ := \frac{\bar{\rho}_w}{\bar{\mu}_w} \sqrt{\frac{\bar{\tau}_w}{\bar{\rho}_w}} (y - y_w); \quad Re_{\tau_w} := \delta^+ \quad (2.1a)$$

fail to correctly represent the major part of the flow, and suggested an alternative y -variable scaling which replaces $\{\bar{\mu}_w, \bar{\rho}_w\}$ by their local values

$$(\cdot)^* \text{ units: } \{\bar{\tau}_w, \bar{\mu}(y), \bar{\rho}(y)\} \implies y^* := \frac{\bar{\rho}(y)}{\bar{\mu}(y)} \sqrt{\frac{\bar{\tau}_w}{\bar{\rho}(y)}} (y - y_w); \quad Re_{\tau^*} := \delta^*. \quad (2.1b)$$

This HCB friction Reynolds number Re_{τ^*} (2.1b) is the appropriate parameter determining the peak value of the shear Reynolds stress $-\overline{\rho u''v''}$ (Huang *et al.* 1995) and is generally accepted as the representative Reynolds number for compressible TPC flow (Trettel & Larsson 2016). However, both scalings (2.1a), (2.1b) become identical at the wall and, in general, neither is well adapted in the near-wall region $y^* \lesssim 10$. In that region, $(\cdot)^*$ -units vary rapidly in the wall-normal direction because of the strong temperature gradient (figure 1). The drawback of this rapid variation was particularly felt in the present work while studying the near-wall pressure field in relation with the near-wall low-speed streaks (§ 4.1). It is shown that, for a given flow defined by the couple $(Re_{\tau^*}, \bar{M}_{CL_x})$, the average spanwise distance between streaks $\Lambda_S^{(z)}$ is practically

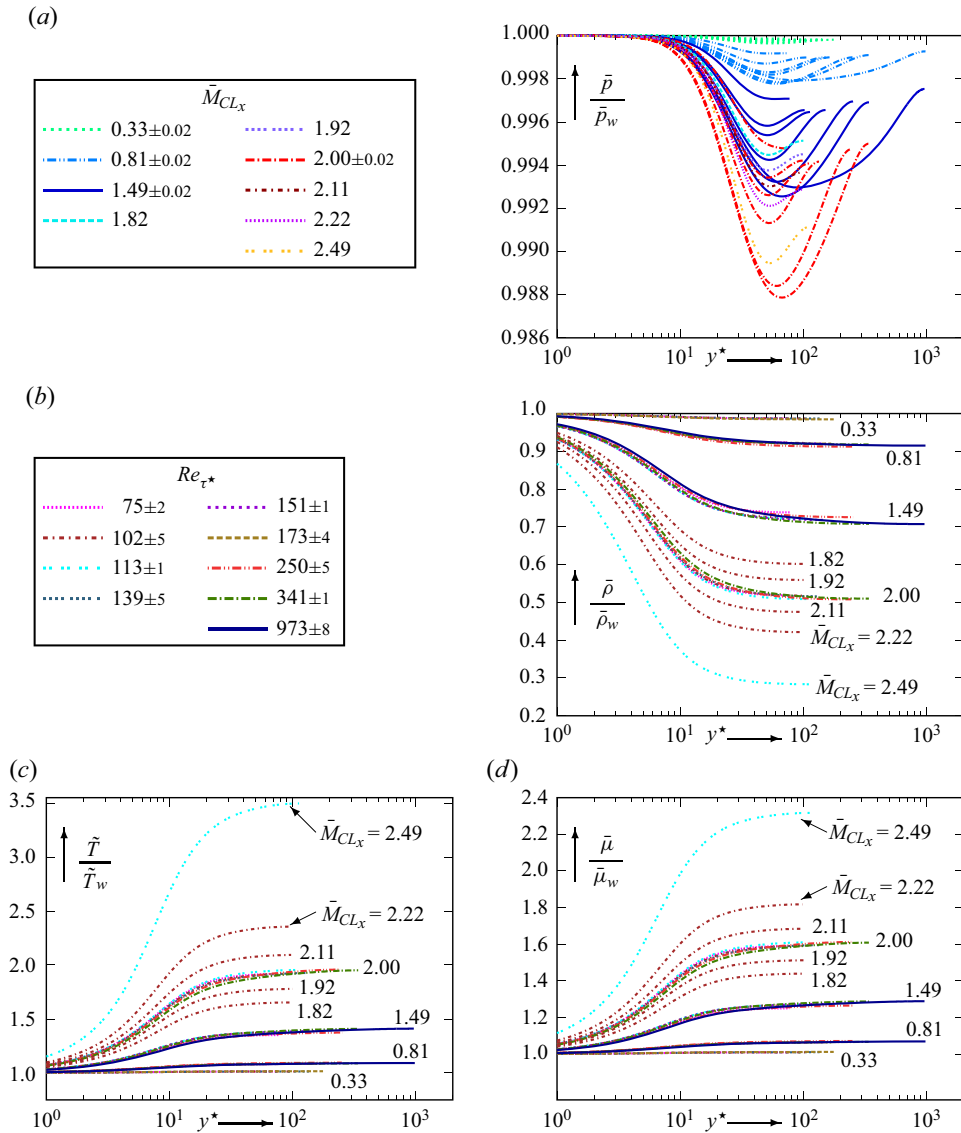


Figure 1. Wall-normal variation of mean thermodynamic variables $\{\bar{p}, \bar{\rho}, \bar{T}, \bar{\mu}\}$ with respect to their wall values, plotted against the HCB-scaled non-dimensional distance from the wall y^* (2.1b), for varying centreline Mach number (2.4) $0.32 \leq \bar{M}_{CL_x} \leq 2.49$ (\bar{M}_{CL_x} -based line types are used for $\bar{p}(y)$) and HCB friction Reynolds number (2.1b) $73 \leq Re_{\tau^*} \leq 983$ (Re_{τ^*} -based line types are used for $\{\bar{\rho}(y), \bar{T}(y), \bar{\mu}(y)\}$), from the present database (table 1).

y -independent in the near-wall region $y^* \lesssim 10$, so that studying the velocity and pressure fields in (x^*, z^*) planes would misleadingly suggest strong y -normal variations in $(\cdot)^*$ -units (2.1b). On the other hand, it was also found that standard $(\cdot)^+$ -units (2.1a) are completely inadequate in comparing results for different \bar{M}_{CL_x} at constant Re_{τ^*} . Noting that the strong variation of mean-flow properties essentially occurs in the region $y^* \lesssim 15$, we found that an alternative y -constant scaling which uses centreline thermodynamic properties $\{\bar{\mu}_{CL}, \rho_{CL}\}$ everywhere performed better. In the TPC case, $\max_y \bar{T} = \bar{T}_{CL}$ occurs at the

centreline, with monotonic decrease towards the wall (figure 1). On the other hand, in the case of adiabatic-wall ZPG TBLs, where $\max_y \bar{T} = \bar{T}_w$ occurs at the wall, with monotonic decrease towards the boundary-layer edge, standard wall-units (2.1a) perform quite well (Bernardini & Pirozzoli 2011; Zhang *et al.* 2017). Both these choices can be accommodated, for the entire cold-wall range $\bar{T}_w/T_r \leq 1$, by

$$(\cdot)^\ddagger \text{ units: } \left\{ \bar{\tau}_w, \max_y \bar{\mu}, \min_y \bar{\rho} \right\} \implies y^\ddagger := \frac{\min_y \bar{\rho}}{\max_y \bar{\mu}} \sqrt{\frac{\bar{\tau}_w}{\min_y \bar{\rho}}} (y - y_w); \quad Re_{\tau^\ddagger} := \delta^\ddagger. \quad (2.1c)$$

Obviously, for TPC (2.2a) or adiabatic-wall conditions (2.2b)

$$\left(\max_y \bar{\mu}, \min_y \bar{\rho} \right) = (\bar{\mu}_{CL}, \bar{\rho}_{CL}) \xrightarrow{(2.1b), (2.1c)} \delta^\ddagger = \delta^* \iff Re_{\tau^\ddagger} = Re_{\tau^*}, \quad (2.2a)$$

$$\left(\max_y \bar{\mu}, \min_y \bar{\rho} \right) = (\bar{\mu}_w, \bar{\rho}_w) \xrightarrow{(2.1a), (2.1c)} \delta^\ddagger = \delta^+ \iff Re_{\tau^\ddagger} = Re_{\tau^+}. \quad (2.2b)$$

Therefore, this y -independent system of mixed (friction/thermodynamics) scaling (2.1c) $(\cdot)^\ddagger$ -units retains $(Re_{\tau^*}, \bar{M}_{CL_x})$ as global flow parameters in canonical compressible TPC flow (2.2a). This point is discussed further in (§ 4).

Note that the unit for p is $\bar{\tau}_w$ in all of these systems (2.1), i.e.

$$(2.1) \implies p^\ddagger \equiv p^* \equiv p^+ := \frac{p}{\bar{\tau}_w}. \quad (2.3)$$

2.2. Computational method and statistics

The computations were run using a very-high-order $O(\Delta \ell^{17})$ upwind-biased scheme (Gerolymos, Sénéchal & Vallet 2009), implemented in a DNS solver (Gerolymos, Sénéchal & Vallet 2010) which has been validated extensively in previous compressible (Gerolymos & Vallet 2014, 2018) and low- \bar{M}_{CL_x} (Gerolymos *et al.* 2013; Gerolymos & Vallet 2016, 2019) work, by comparison with standard DNS data (Coleman *et al.* 1995; Moser, Kim & Mansour 1999; Foysi *et al.* 2004; Vreman & Kuerten 2014), including spectra (Gerolymos *et al.* 2010) and higher-order-derivatives dissipation statistics (Gerolymos & Vallet 2016).

The computational box was $L_x = 8\pi\delta$ long in the streamwise direction and $L_z = 4\pi\delta$ wide in the spanwise direction (δ is the channel half-height), which is in the upper range of DNS computational domains for channel flow both compressible (Modesti & Pirozzoli 2016; Trettel & Larsson 2016; Tang *et al.* 2020; Yu *et al.* 2019, 2020; Yu & Xu 2021) and incompressible (Kim, Moin & Moser 1987; Moser *et al.* 1999; Hu & Sandham 2001; Hoyas & Jiménez 2006; Lee & Moser 2015; Hoyas *et al.* 2022). Computational resolution in wall-units (table 1) is typical of compressible TPC flow DNS computations, in line with grid-resolution studies (Gerolymos *et al.* 2010; Modesti & Pirozzoli 2016; Trettel & Larsson 2016).

Some early computations in the database (Gerolymos & Vallet 2014, 2018) were initialised following the procedure described in Gerolymos *et al.* (2010, (44), p. 790). However, most of the computations were initialised by thermodynamic rescaling and linear interpolation of an instantaneous turbulent flow field at different $(Re_{\tau^*}, \bar{M}_{CL_x})$ -conditions.

Computational experience shows that p'_{rms} reaches statistical convergence much slower than velocity covariances and other statistics. For this reason we were particularly

$$L_x \times L_y \times L_z = 8\pi\delta \times 2\delta \times 4\pi\delta; \quad T_w = 298 \text{ K} = \text{const.}$$

Re_{τ^*}	\bar{M}_{CL_x}	Re_{τ_w}	M_{B_w}	$N_x \times N_y \times N_z$	Δx^+	Δy_w^+	$N_{y^+ \leq 10}$	Δy_{CL}^+	Δz^+	$\Delta t^+ = \Delta t_s^+$	t_{OBS}^+
66	1.63	102	1.51	137 × 113 × 201	18.8	0.18	22	3.2	6.4	0.012211	17901
74	0.33	75	0.27	201 × 121 × 321	9.4	0.12	27	2.2	2.9	0.003432	8356
74	0.81	82	0.67	201 × 121 × 321	10.3	0.13	26	2.4	3.2	0.005122	9683
77	1.49	112	1.40	201 × 121 × 321	14.1	0.17	23	3.3	4.4	0.008526	11455
75	2.05	166	2.26	321 × 145 × 505	13.0	0.20	23	4.1	4.1	0.011309	11011
103	1.51	153	1.47	401 × 169 × 557	9.6	0.12	29	3.1	3.5	0.005365	7391
100	1.82	186	1.93	401 × 169 × 557	11.7	0.15	26	3.7	4.2	0.008541	7646
100	1.92	203	2.11	401 × 169 × 557	12.8	0.17	25	4.1	4.6	0.009865	9294
99	2.01	219	2.30	401 × 169 × 557	13.7	0.18	24	4.4	4.9	0.011064	6555
97	2.11	238	2.50	401 × 169 × 557	14.9	0.19	23	4.8	5.4	0.012502	9586
98	2.22	276	2.79	401 × 169 × 557	17.3	0.22	22	5.5	6.2	0.015354	8107
105	0.32	107	0.27	257 × 129 × 385	10.5	0.17	23	2.7	3.5	0.005187	7785
106	0.79	117	0.69	257 × 129 × 385	11.5	0.18	22	3.0	3.8	0.013823	9095
114	1.51	170	1.49	257 × 129 × 385	16.7	0.22	21	4.7	5.6	0.015161	10494
112	2.02	252	2.35	457 × 177 × 633	13.9	0.18	24	4.9	5.0	0.010082	6326
113	2.49	491	3.84	801 × 241 × 1201	15.4	0.18	21	5.4	5.1	0.004418	6627
143	0.32	145	0.28	257 × 129 × 385	14.3	0.19	22	4.0	4.8	0.005032	7789
134	1.99	298	2.33	481 × 181 × 745	15.6	0.18	23	5.1	5.0	0.010065	7601
151	0.79	168	0.70	421 × 149 × 801	10.0	0.17	23	3.7	2.6	0.011671	7060
151	1.50	228	1.51	345 × 137 × 529	16.6	0.23	19	5.7	5.4	0.016631	9564
169	0.79	187	0.71	421 × 149 × 801	11.2	0.19	22	4.1	2.9	0.012918	7673
177	0.35	180	0.30	257 × 129 × 385	17.7	0.23	20	5.0	5.9	0.006551	9695
251	0.83	282	0.75	633 × 177 × 1201	11.2	0.18	24	5.3	2.9	0.011526	5902
254	1.47	377	1.49	585 × 209 × 881	16.2	0.20	20	4.8	5.4	0.012121	6121
245	1.99	555	2.39	1201 × 281 × 1601	11.6	0.19	23	5.2	4.4	0.010531	7373
340	0.80	378	0.72	593 × 233 × 889	16.0	0.19	22	4.3	5.3	0.011236	7285
342	1.51	523	1.56	801 × 241 × 1201	16.4	0.20	21	5.7	5.5	0.010854	6558
341	1.98	768	2.39	1441 × 281 × 2001	13.4	0.20	22	7.3	4.8	0.009052	4973
983	0.81	1099	0.74	2145 × 481 × 2689	12.9	0.20	28	6.2	5.1	0.009005	2923
965	1.51	1478	1.57	2849 × 641 × 3473	13.0	0.21	30	6.1	5.4	0.012139	5346

Table 1. Parameters of the DNS computations: L_x, L_y, L_z (N_x, N_y, N_z) are the dimensions (number of grid points) of the computational domain (x = homogeneous streamwise, y = wall-normal, z = homogeneous spanwise direction); u, v, w are the velocity components along x, y, z ; δ is the channel half-height; $\Delta x^+, \Delta y_w^+, \Delta y_{CL}^+, \Delta z^+$ are the mesh sizes in wall-units (2.1a); $(\cdot)_w$ denotes wall and $(\cdot)_{CL}$ centreline values; $N_{y^+ \leq 10}$ is the number of grid points between the wall and $y^+ = 10$; Re_{τ^*} is the friction Reynolds number in HCB scaling (2.1b); \bar{M}_{CL_x} is the centreline Mach number (2.4); Re_{τ_w} is the friction Reynolds number (2.1a); M_{B_w} is the bulk Mach number at wall sound speed (§ 2.3); Δt^+ is the computational time step in wall-units; t_{OBS}^+ is the observation interval in wall-units over which single-point statistics were computed; Δt_s^+ is the sampling time step for the single-point statistics in wall-units.

careful to allow for a sufficiently long transient t_{CNVRG} . Upon reaching a statistically converged state, after the initial transient, single-point statistics were acquired at each time step and sampled over several thousands of time wall-units (table 1). For the $(Re_{\tau^*}, \bar{M}_{CL_x}) = (965, 1.50)$ flow, initialised from a statistically converged coarse-grid flow field, after a transient of $t_{CNVRG}^+ = 9853$ ($t_{CNVRG} \tilde{u}_{CL} / \delta = 180$), statistics were acquired for an additional $t_{OBS}^+ = 5346$ ($t_{OBS} \tilde{u}_{CL} / \delta = 98$).

Air thermodynamics were approximated by a perfect gas EoS with Sutherland laws for viscosity and heat conductivity (Gerolymos & Vallet 2014, (2.1), p. 706). van Driest (1951, figure 17, p. 157) highlights the overestimation of dynamic viscosity at high temperatures when using a power law in lieu of the more accurate Sutherland’s law. Since temperature stratification is induced by viscous heating $\overline{S_{ij}\tau_{ij}}$ (Coleman *et al.* 1995) there are small differences at high \bar{M}_{CL_x} in centreline-to-wall temperature ratio \bar{T}_{CL}/T_w and in the $M_{B_w}(Re_{\tau^*}, \bar{M}_{CL_x})$ relation between DNS data using different laws for viscosity. This observation notwithstanding, the present results using Sutherland’s law are in very good agreement with the p'_{rms} data of Modesti & Pirozzoli (2016) who used a power law, for flows at similar $(Re_{\tau^*}, \bar{M}_{CL_x})$ conditions.

2.3. Database

The target during the construction of the database was to obtain a matrix of $(Re_{\tau^*}, \bar{M}_{CL_x})$ values, where Re_{τ^*} is the HCB friction Reynolds number (2.1b) and

$$\bar{M}_{CL_x} := \left(\frac{u_{CL}}{a_{CL}} \right) \tag{2.4}$$

is the average streamwise centreline Mach number. Note that the often used approximations $\bar{M}_{CL} \approx \bar{M}_{CL_x} \approx \tilde{u}_{CL}/a(\bar{T}_{CL})$ are confirmed by the data with good accuracy because $v_{CL} \ll u_{CL} \gg w_{CL}$ and $(T'_{rms}/\bar{T})_{CL} \lll 1$. We use the exact average (2.4) in our work.

In general, Re_{τ^*} is adopted by workers in the field (§ 2.1), because it is the proper parameter for the scaling of the Reynolds shear stress $-\overline{\rho u''v''}$ and, hence, controls the mean velocity \tilde{u} profile (Trettel & Larsson 2016). We chose the centreline Mach number \bar{M}_{CL_x} for the matrix construction because it allows comparison with boundary-layer data which are always referenced to the external flow Mach number, and because its physical significance is clear. Furthermore the coefficients of variation $CV_{(\cdot)'} := (\cdot)'_{rms}/\overline{(\cdot)}$ of the thermodynamic fluctuations $\{p', \rho', T', s'\}$ scale with $\bar{M}_{CL_x}^2$ (Gerolymos & Vallet 2014, 2018).

Neither Re_{τ^*} nor \bar{M}_{CL_x} are fixed in the computations, the flow conditions being determined by the set $\{\rho_B, \dot{m}_B, \bar{T}_w\}$ (Gerolymos *et al.* 2010), where $\rho_B := \bar{\rho}^{xyz}$ is the bulk density, $\dot{m}_B := L_y L_z \rho_B u_B := L_y L_z \bar{\rho} u^{xyz}$ is the mass flow, and $T_w = \text{const.}$ is the wall temperature (as a consequence the bulk-wall Mach number $M_{B_w} := u_B/\bar{a}_w$ is fixed).

However, we took particular care in the construction of the database to obtain the closest possible target $\bar{M}_{CL_x} \in \{0.33, 0.80, 1.50, 2.00\}$ and $Re_{\tau^*} \in \{75, 100, 110, 250, 340, 1000\}$ (table 1). The cost of the computations strongly increases with \bar{M}_{CL_x} if nearly constant resolution in standard wall-units is sought (this is the most stringent resolution assessment), as a result of the rapid increase of the ratio Re_{τ_w}/Re_{τ^*} with increasing \bar{M}_{CL_x} . This new database (table 1) extends available data at $\bar{M}_{CL_x} \in \{0.8, 1.5\}$ to higher $Re_{\tau^*} \approx 1000$, which to the best of the authors’ knowledge is the highest reported Re_{τ^*} for compressible TPC flow.

3. p'^+_{rms} scaling

It is well established that $[p'_{rms}]_w^+ := \sqrt{\overline{(p')^2}}_w^+$ increases with Re_{τ_w} both for incompressible (Panton *et al.* 2017; Chen & Sreenivasan 2022) and supersonic (Bernardini &

Pirozzoli 2011) wall turbulence. On the other hand, at constant Re_{τ^*} , the coefficient of variation $(CV_{p'})_w := (p'_{rms}/\bar{p})_w$ scales approximately with $\bar{M}_{CL_x}^2$ in compressible TPC flow (Gerolymos & Vallet 2014, 2018). We concentrate in § 3 on the combined $(Re_{\tau^*}, \bar{M}_{CL_x})$ effect on p' , and in § 3.4 we attempt to identify independently the relative importance of Mach number \bar{M}_{CL_x} and wall cooling T_r/\bar{T}_w .

3.1. Wall-pressure-fluctuation amplitude

When plotting (figure 2) the compressible data vs Re_{τ_w} (2.1a) we observe similar curves for different \bar{M}_{CL_x} , shifted towards lower levels of $[p'_{rms}]_w^+$ with increasing \bar{M}_{CL_x} , highlighting a distinct \bar{M}_{CL_x} -dependence. Using instead the HCB friction Reynolds number Re_{τ^*} (2.1b) clusters the data much closer together (figure 2). Nonetheless, careful observation shows that there remains a weak \bar{M}_{CL_x} -dependence, which appears clearly when plotting the data for different nearly constant Re_{τ^*} versus \bar{M}_{CL_x} (figure 2). At constant Re_{τ^*} , $[p'_{rms}]_w^+$ slightly increases with increasing \bar{M}_{CL_x} , relative to the incompressible flow limit ($\bar{M}_{CL_x} \rightarrow 0$) level (figure 2).

Carefully choosing the appropriate Reynolds and Mach number definitions, can only diminish the influence of one of the two parameters, but not altogether remove it: compressible TPC flow is biparametric.

3.2. p'_{rms} profiles

The profiles of p'_{rms} at nearly constant $\bar{M}_{CL_x} \in \{0.33, 0.80, 1.50, 2.00\}$ (figure 3) show an increase in the level of p' with increasing Re_{τ^*} , quite similar to the incompressible flow behaviour (Panton *et al.* 2017; Chen & Sreenivasan 2022). However, considering the effect of \bar{M}_{CL_x} at nearly constant $Re_{\tau^*} \in \{100, 110, 250, 340\}$ shows that in the near-wall region, which can be defined as $y^* \lesssim 15$, the level of p' is strongly dependent on the Mach number.

At the incompressible flow limit, the maximal value of p'_{rms} is located in the range $29 \lesssim y^* \lesssim 32$ (depending on the Reynolds number). We can define this peak value as a local maximum of the p'_{rms} profile

$$[p'_{rms}]_{PEAK}^+ := \text{local max}_{y>0} p'_{rms}^+. \quad (3.1)$$

With increasing \bar{M}_{CL_x} the wall level $[p'_{rms}]_w$ increases relative to the peak $[p'_{rms}]_{PEAK}$. The data for $Re_{\tau^*} \approx 100$ show (figure 3) that at $\bar{M}_{CL_x} \approx 1.9$ the decrease from $[p'_{rms}]_{PEAK}$ to the wall ceases to be monotonic, but instead the profile forms a local minimum before increasing again towards the wall. This increase becomes more pronounced with increasing \bar{M}_{CL_x} and, at $\bar{M}_{CL_x} \approx 2.3$, $[p'_{rms}]_w$ rises slightly higher than $[p'_{rms}]_{PEAK}$ (figure 3). For the case $(Re_{\tau^*}, \bar{M}_{CL_x}) = (113, 2.49)$ (figure 3) the wall level is clearly higher than the local maximum $[p'_{rms}]_{PEAK}$ (3.1). This \bar{M}_{CL_x} effect is confirmed by the higher $Re_{\tau^*} \in \{250, 341\}$ data (figure 3) which follow the same trend. The p'_{rms} profiles are better understood by non-dimensionalising by the peak value $[p'_{rms}]_{PEAK}$ (3.1), thereby correcting for the slight scatter imparted to the data by the small variations of Re_{τ^*} around the nominal target values of $\{100, 110, 250, 341\}$ (figure 3).

Note that the centreline region (figure 3) shows a consistent \bar{M}_{CL_x} -effect, the centreline level $[p'_{rms}]_{CL}^+$ increasing with increasing \bar{M}_{CL_x} , at constant Re_{τ^*} .

Pressure fluctuations in compressible wall turbulence

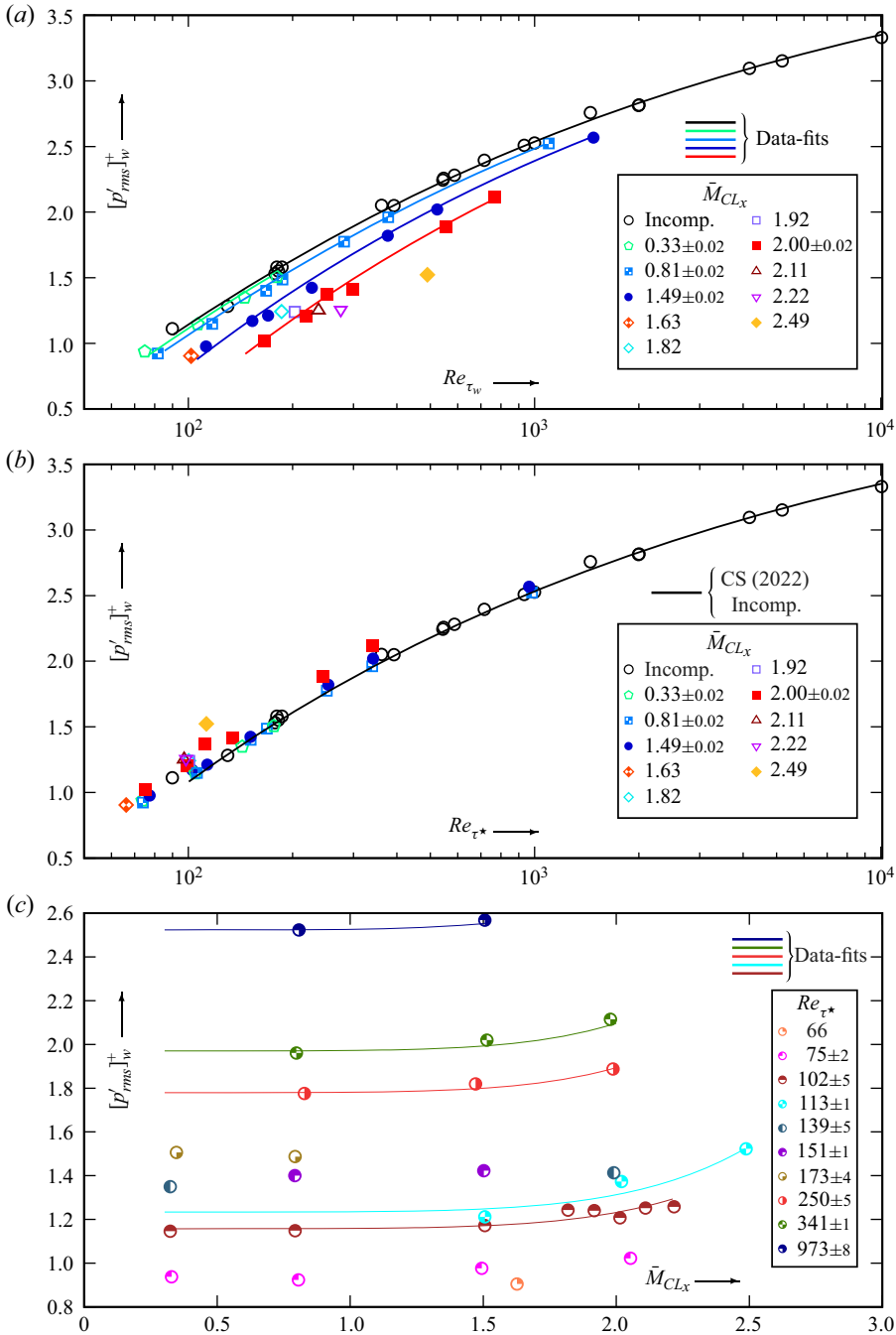


Figure 2. Wall pressure fluctuation r.m.s. $[p'_{rms}]_w^+$, in wall-units (2.3), plotted against the friction Reynolds numbers Re_{τ_w} (2.1a) and Re_{τ^*} (2.1b), for varying Mach numbers $0.32 \leq \bar{M}_{CLx} \leq 2.49$, and against the centreline Mach number \bar{M}_{CLx} (2.4), for varying Reynolds numbers $66 \leq Re_{\tau^*} \leq 983$, from the present database (table 1); also included are incompressible DNS data (Kim *et al.* 1987; Moser *et al.* 1999; Hu & Sandham 2001; Hoyas & Jiménez 2006; Lee & Moser 2015; Hoyas *et al.* 2022) and incompressible-flow correlation (Chen & Sreenivasan 2022) using Re_{τ^*} (CS, 2022).

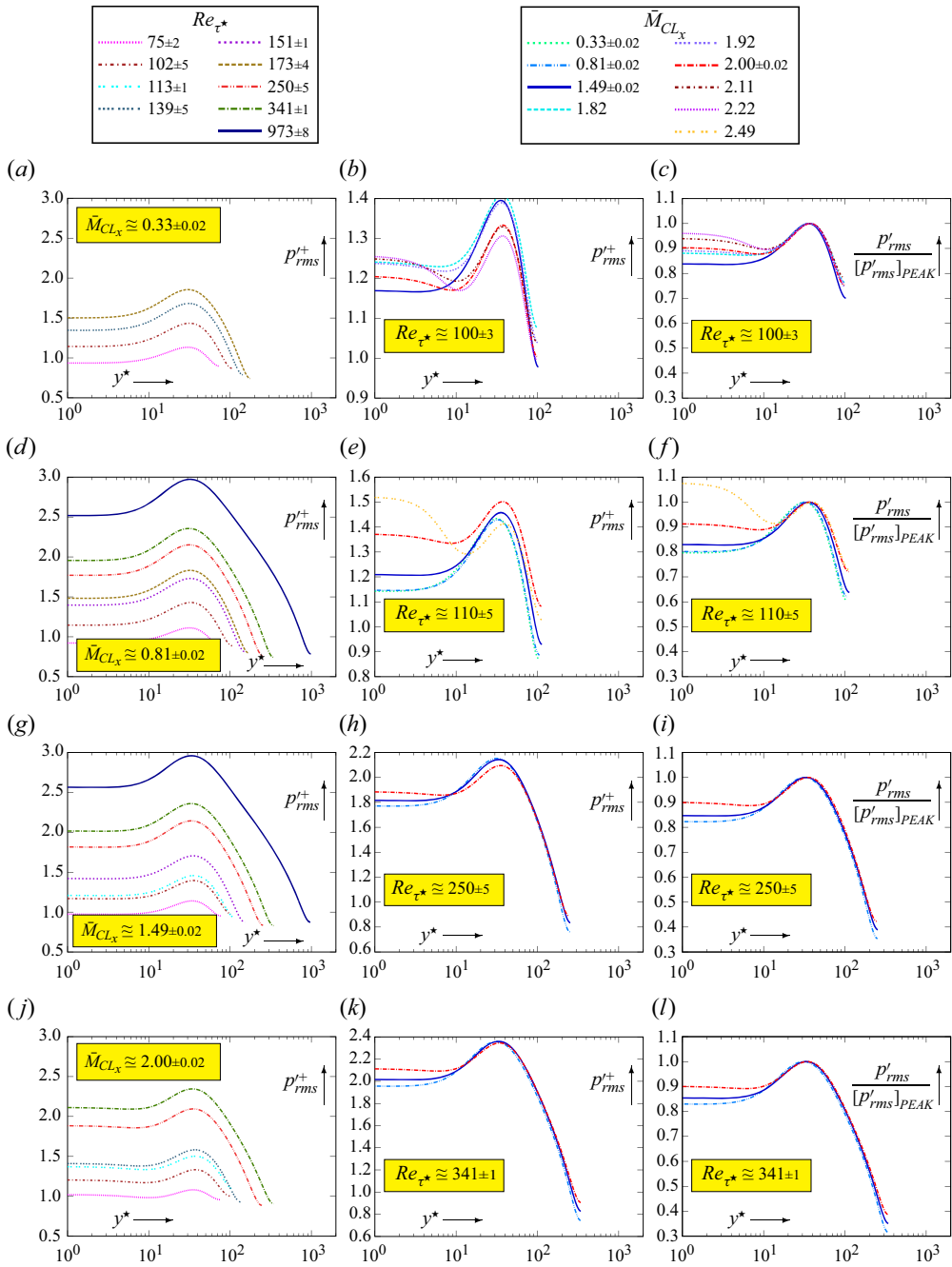


Figure 3. Profiles of pressure-fluctuation r.m.s. p'_{rms+} , in wall-units (2.3), plotted against the HCB-scaled (2.1b) non-dimensional distance from the wall y^* (logscale), for varying $73 \leq Re_{\tau^*} \leq 965$ at nearly constant $\bar{M}_{CL_x} \in \{0.33, 0.80, 1.50, 2.00\}$ and for varying $0.32 \leq \bar{M}_{CL_x} \leq 2.49$ at nearly constant $Re_{\tau^*} \in \{100, 110, 250, 340\}$ (also scaled by its peak value, $[p'_{rms+}]_{PEAK}$ (3.1), for the different nearly constant Re_{τ^*}), from the present DNS database (table 1).

Pressure fluctuations in compressible wall turbulence

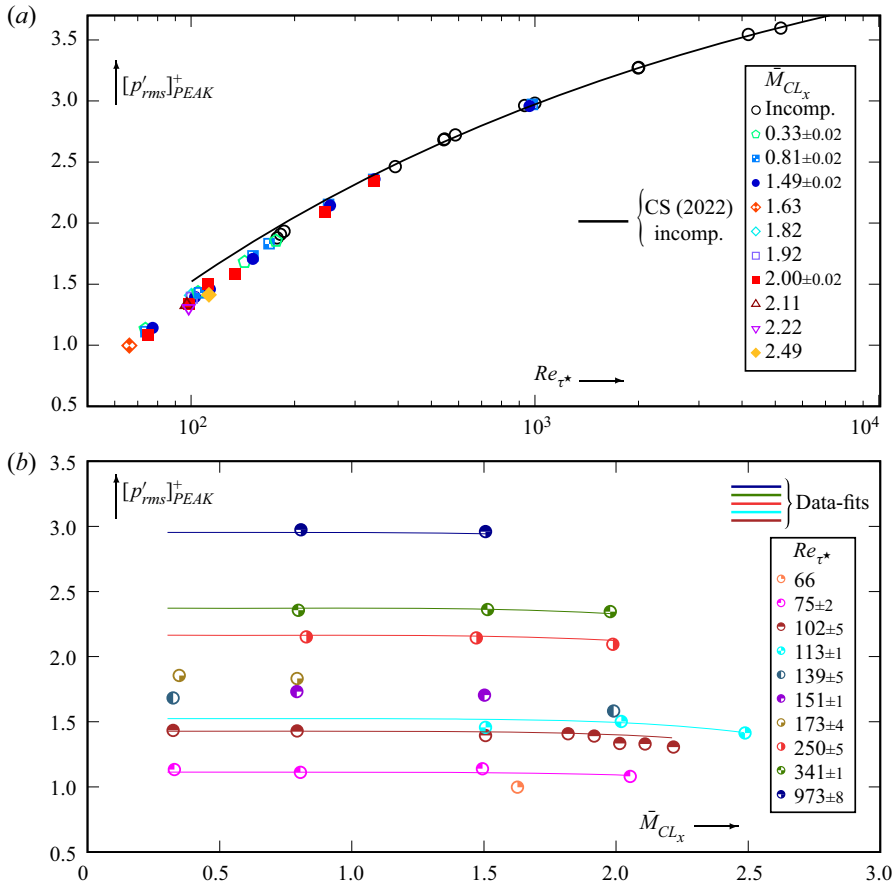


Figure 4. Peak value of pressure-fluctuation r.m.s. $[p'_{rms}]_{PEAK}^+$ (3.1), in wall-units (2.3), plotted against Re_{τ^*} (2.1b), for varying $0.32 \leq \bar{M}_{CL_x} \leq 2.49$, and against \bar{M}_{CL_x} (2.4), for varying $66 \leq Re_{\tau^*} \leq 983$, from the present database (table 1); also included are incompressible DNS data (Kim *et al.* 1987; Moser *et al.* 1999; Hu & Sandham 2001; Hoyas & Jiménez 2006; Lee & Moser 2015) and incompressible-flow correlation (Chen & Sreenivasan 2022) using Re_{τ^*} (CS, 2022).

3.3. p'_{rms} peak

The data for $[p'_{rms}]_{PEAK}^+$ (figure 4), with varying Re_{τ^*} at different \bar{M}_{CL_x} , are quite close to the incompressible DNS data (indeed closer compared with $[p'_{rms}]_w^+$; figure 2). There is, at constant Re_{τ^*} , a small decrease with \bar{M}_{CL_x} (figure 4), but notably smaller than the \bar{M}_{CL_x} -dependence of the wall value $[p'_{rms}]_w^+$ (figure 2).

The location of the peak

$$y_{p'_{PEAK}}^* := y^* |_{[p'_{rms}]_{PEAK}} \quad (3.2)$$

was obtained by interpolating the discrete on-grid data by a degree-four polynomial in the neighbourhood of the discrete maximum, to avoid grid-dependent scatter ($[p'_{rms}]_{PEAK}^+$ is the value of the interpolating polynomial at $y_{p'_{PEAK}}^*$).

The location of the peak $y_{p'_{PEAK}}^*$ (3.2) varies both with Re_{τ^*} and \bar{M}_{CL_x} (figure 5). The dependence on Re_{τ^*} is similar to that observed in the incompressible flow data

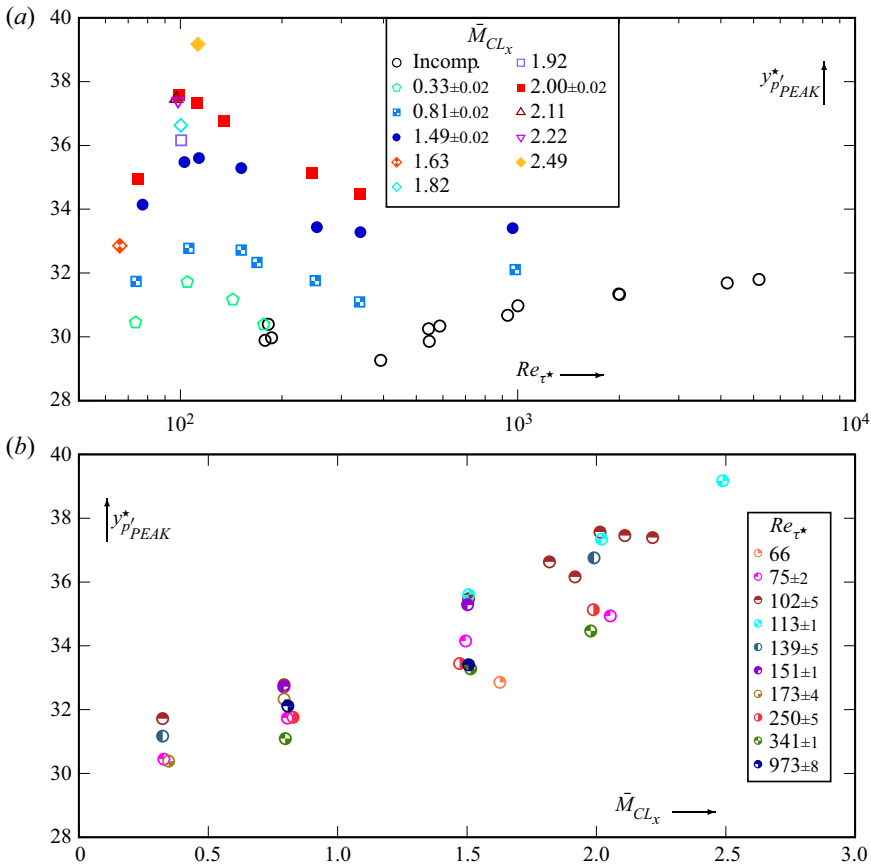


Figure 5. HCB-scaled (2.1b) non-dimensional distance from the wall of the p'_{rms} peak (3.1) location, $y_{p'PEAK}^*$ (3.2), plotted against Re_{τ^*} (2.1b), for varying Mach numbers $0.32 \leq \bar{M}_{CL_x} \leq 2.49$ and against \bar{M}_{CL_x} (2.4), for varying $66 \leq Re_{\tau^*} \leq 983$, from the present database (table 1); also included are incompressible DNS data (Kim *et al.* 1987; Moser *et al.* 1999; Hu & Sandham 2001; Hoyas & Jiménez 2006; Lee & Moser 2015).

(figure 5). In the transitional flow range $Re_{\tau^*} \lesssim 100$ the peak moves away from the wall with increasing Re_{τ^*} , reaching a local maximum around $100 \lesssim Re_{\tau^*} \lesssim 110$, i.e. at the Re_{τ^*} -range which marks the end of transition. At higher Re_{τ^*} , $y_{p'PEAK}^*$ initially decreases towards a local minimum around $Re_{\tau^*} \approx 400$, to slowly increase again, possibly towards an asymptotic value (figure 5). The variation of $y_{p'PEAK}^*$ vs Re_{τ^*} appears to be quite similar for different \bar{M}_{CL_x} but shifted towards higher values with increasing \bar{M}_{CL_x} (figure 5). The location of the peak $y_{p'PEAK}^*$ (3.2) is much more sensitive to variations of \bar{M}_{CL_x} than of Re_{τ^*} (figure 5). Note, however, that the p'_{rms} profiles are quite flat in the neighbourhood of the peak (figure 3).

3.4. Relative importance of T_r/\bar{T}_w and \bar{M}_{CL_x} on the near-wall field

The data for the \bar{M}_{CL_x} -dependance of $[p'_{rms}]_w^+$ (figure 2) reflect the combined influence of increasing Mach number \bar{M}_{CL_x} and wall cooling T_r/\bar{T}_w , which increases very rapidly with \bar{M}_{CL_x} in TPC where frictional heating can only be evacuated through the walls (figure 6).

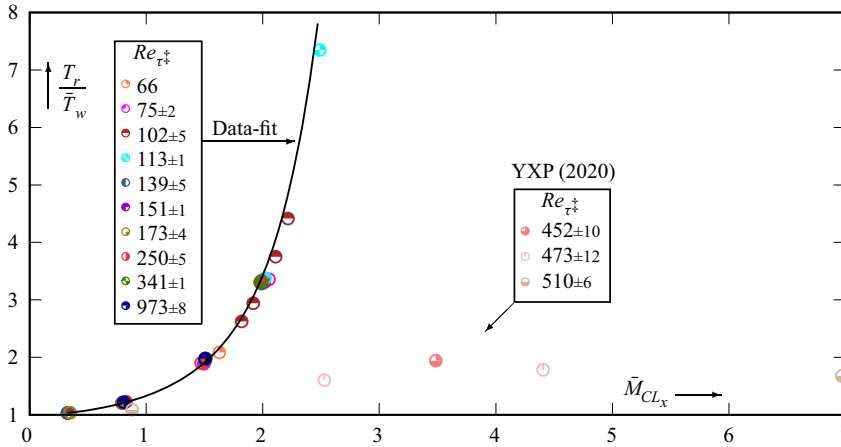


Figure 6. Variation of wall-cooling ratio $1 < T_r/\bar{T}_w \lesssim 7.35$ ($0.136 \lesssim \bar{T}_w/T_r < 1$) and centreline Mach number $0.32 \lesssim \bar{M}_{CLx} \lesssim 6.97$ for the present data (table 1) and for the Yu *et al.* (2019, 2020) DNS data (YXP, 2020), for varying $66 \leq Re_{\tau^+} \leq 983$.

The data of Yu *et al.* (2020) with an artificial sink term in the energy equation extend the \bar{M}_{CLx} range with weakly cooled walls (figure 6).

A working correlation should be a function of the three parameters $\{Re_{\tau^+}, \bar{M}_{CLx}, T_r/\bar{T}_w\}$. The correlation (figure 7)

$$[p'_{rms}]_w^+ = \underbrace{\left(4.4 - 10.5Re_{\tau^+}^{-1/4}\right)}_{[p'_{rms}]_{w,INC}^+(Re_{\tau^+})} \underbrace{\left(\frac{1 + 0.020\bar{M}_{CLx}^2}{1 + 0.011\bar{M}_{CLx}^2}\right)}_{g_{p'_w}(\bar{M}_{CLx}, T_r/\bar{T}_w)} \left(1 + 0.020\left(\frac{T_r}{\bar{T}_w} - 1\right)\right) \quad (3.3)$$

scales the incompressible-flow correlation of Chen & Sreenivasan (2022) $[p'_{rms}]_{w,INC}^+(Re_{\tau^+})$ with a separable function $g_{p'_w}(\bar{M}_{CLx}, T_r/\bar{T}_w) = g_{M,p'_w}(\bar{M}_{CLx})g_{T,p'_w}(T_r/\bar{T}_w)$. The choice of Re_{τ^+} (2.1c) is made to bridge the present very-cold-wall TPC data with the mildly-cold-wall data of Yu *et al.* (2020), $\max_y \bar{T}$ progressively moving from the centreline towards the wall as adiabatic conditions are approached. The pure Mach-number effect $g_{M,p'_w}(\bar{M}_{CLx})$ cannot be isolated from the available TPC data, and was instead evaluated from adiabatic TBL data (Bernardini & Pirozzoli 2011), the rational function ensuring \bar{M}_{CLx}^2 -dependence at low-Mach conditions while avoiding unbounded increase at high-Mach conditions. Dividing the TPC data by $g_{M,p'_w}(\bar{M}_{CLx})$ indicated a nearly linear trend with increasing wall cooling (with $\pm 5\%$ scatter), suggesting the form of $g_{T,p'_w}(T_r/\bar{T}_w)$. The final correlation (3.3) fits the available data reasonably well (figure 7). Although available data are limited regarding the independent effects of Mach number and wall cooling, the satisfactory collapse of the compressible data on the incompressible correlation supports the view that both effects are important, and both tend to increase $[p'_{rms}]_w^+$ relative to its incompressible-isothermal level at the same Re_{τ^+} .

Regarding the data of Yu *et al.* (2020) the actual $T_r := \bar{T}_{CL}(1 + r_f((\gamma - 1)/2)\bar{M}_{CLx}^2)$ of the statistically converged flow was used (the tabulated data refer to T_r of a virtual flow used for the initialisation and boundary conditions).

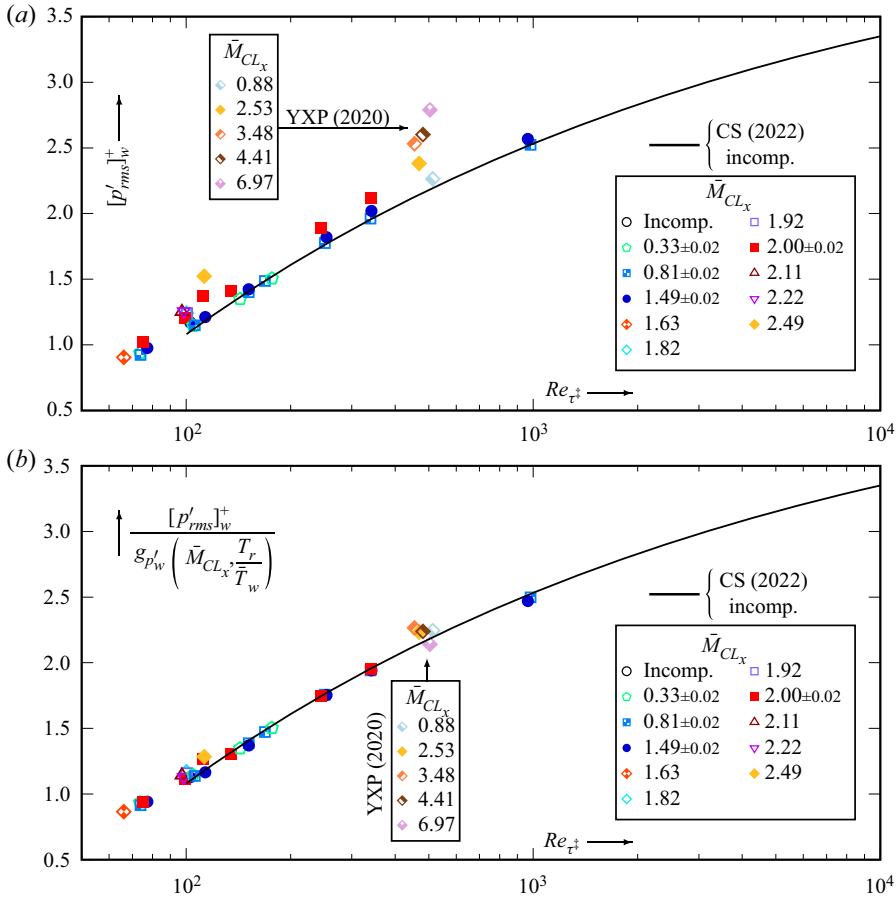


Figure 7. Wall-pressure-fluctuation r.m.s. $[p'_{rms}]_w^+$, in wall-units (2.3) and scaled by $g_{p'_w}(\bar{M}_{CL_x}, T_r/\bar{T}_w)$ (3.3), plotted against the modified friction Reynolds number $66 \leq Re_{\tau^*} \leq 983$ (2.1c), for varying Mach numbers $0.32 \leq \bar{M}_{CL_x} \leq 6.97$ and wall-cooling ratio $1 < T_r/\bar{T}_w \lesssim 7.35$ ($0.136 \lesssim \bar{T}_w/T_r < 1$), from the present database (table 1) and for the Yu *et al.* (2019, 2020) DNS data (YXP, 2020); also included is incompressible-flow correlation (Chen & Sreenivasan 2022) using Re_{τ^*} (CS, 2022).

3.5. Pressure–velocity correlations

Modifications of near-wall turbulence structure (Bradshaw 1977) associated with these \bar{M}_{CL_x} -effects on p'_{rms} (§ 3) can be assessed by considering correlation coefficients between fluctuating pressure and velocity components

$$c_{p'u'} := \frac{\overline{p'u'}}{\sqrt{\overline{p'^2}}\sqrt{\overline{u'^2}}} \equiv \frac{\overline{p'u'}}{p'_{rms}u'_{rms}}; \quad c_{p'v'} := \frac{\overline{p'v'}}{\sqrt{\overline{p'^2}}\sqrt{\overline{v'^2}}} \equiv \frac{\overline{p'v'}}{p'_{rms}v'_{rms}}. \quad (3.4a,b)$$

In general, for all of the $(Re_{\tau^*}, \bar{M}_{CL_x})$ flow conditions in the database (table 1), $c_{p'u'} > 0$ for all $y^* \in]0, \delta^*]$ (figure 8), whereas $c_{p'v'} < 0$ for all $y^* \in]0, \delta^*[$ (figure 9), with $[c_{p'v'}]_{CL} = 0$ because of symmetry.

In the near-wall region ($y^* \lesssim 15$) $c_{p'u'}$, at constant \bar{M}_{CL_x} , shows weak dependence on Re_{τ^*} (figure 8). On the other hand, as \bar{M}_{CL_x} increases above 0.8, at constant Re_{τ^*} , the near-wall level of $c_{p'u'}$ also increases indicating that compressibility effects enhance

Pressure fluctuations in compressible wall turbulence

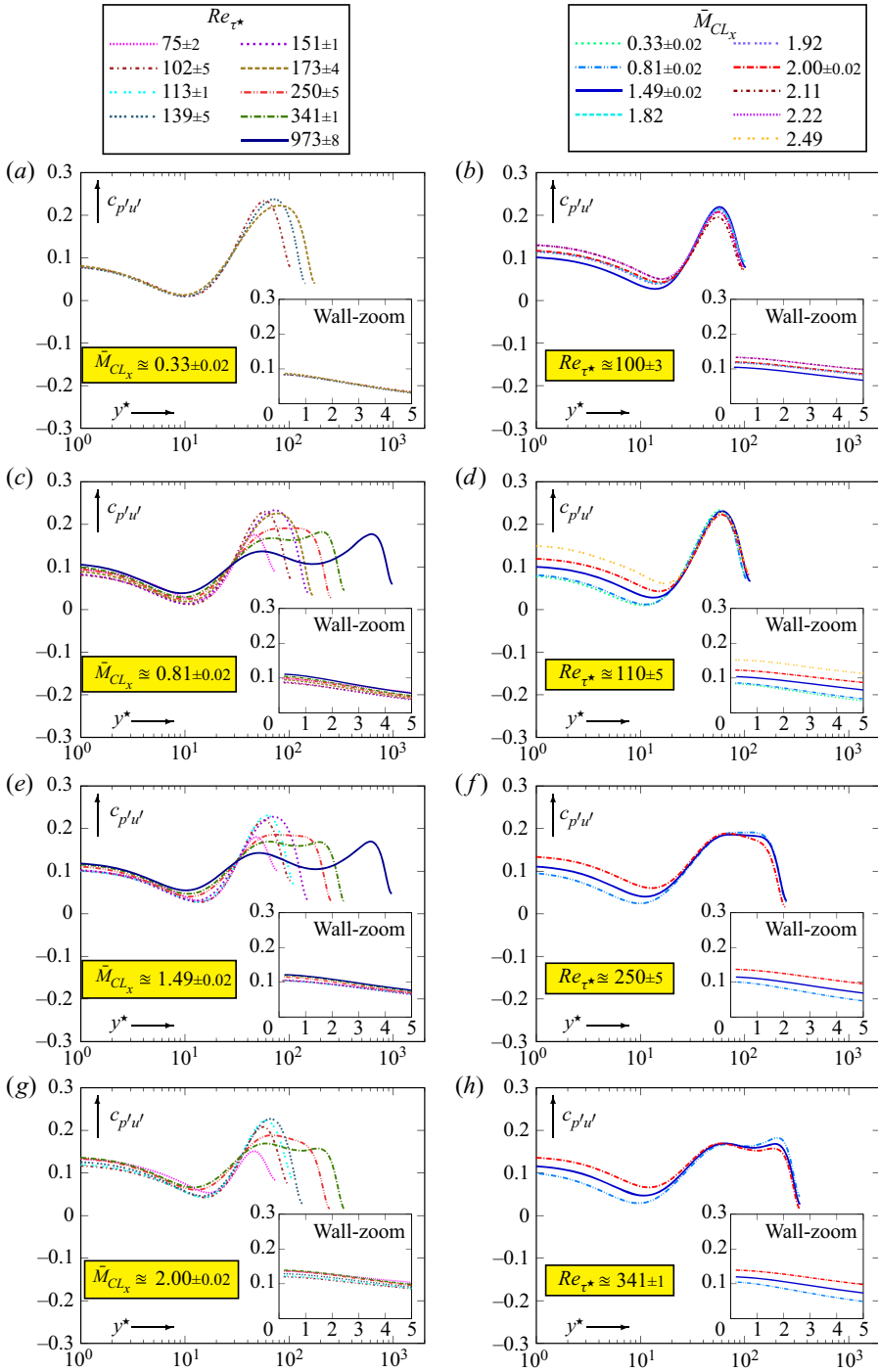


Figure 8. Profiles of correlation coefficient $c_{p'u'}$ of streamwise pressure transport (3.4a,b), plotted against the HCB-scaled non-dimensional distance from the wall y^* (logscale and linear wall-zoom), for varying HCB Reynolds numbers $73 \leq Re_{\tau^*} \leq 983$ at constant centreline Mach numbers $\bar{M}_{CL_x} \in \{0.33, 0.80, 1.50, 2.00\}$, and for varying centreline Mach numbers $0.32 \leq \bar{M}_{CL_x} \leq 2.49$ at constant HCB Reynolds numbers $Re_{\tau^*} \in \{100, 110, 250, 340\}$, from the present DNS database (table 1).

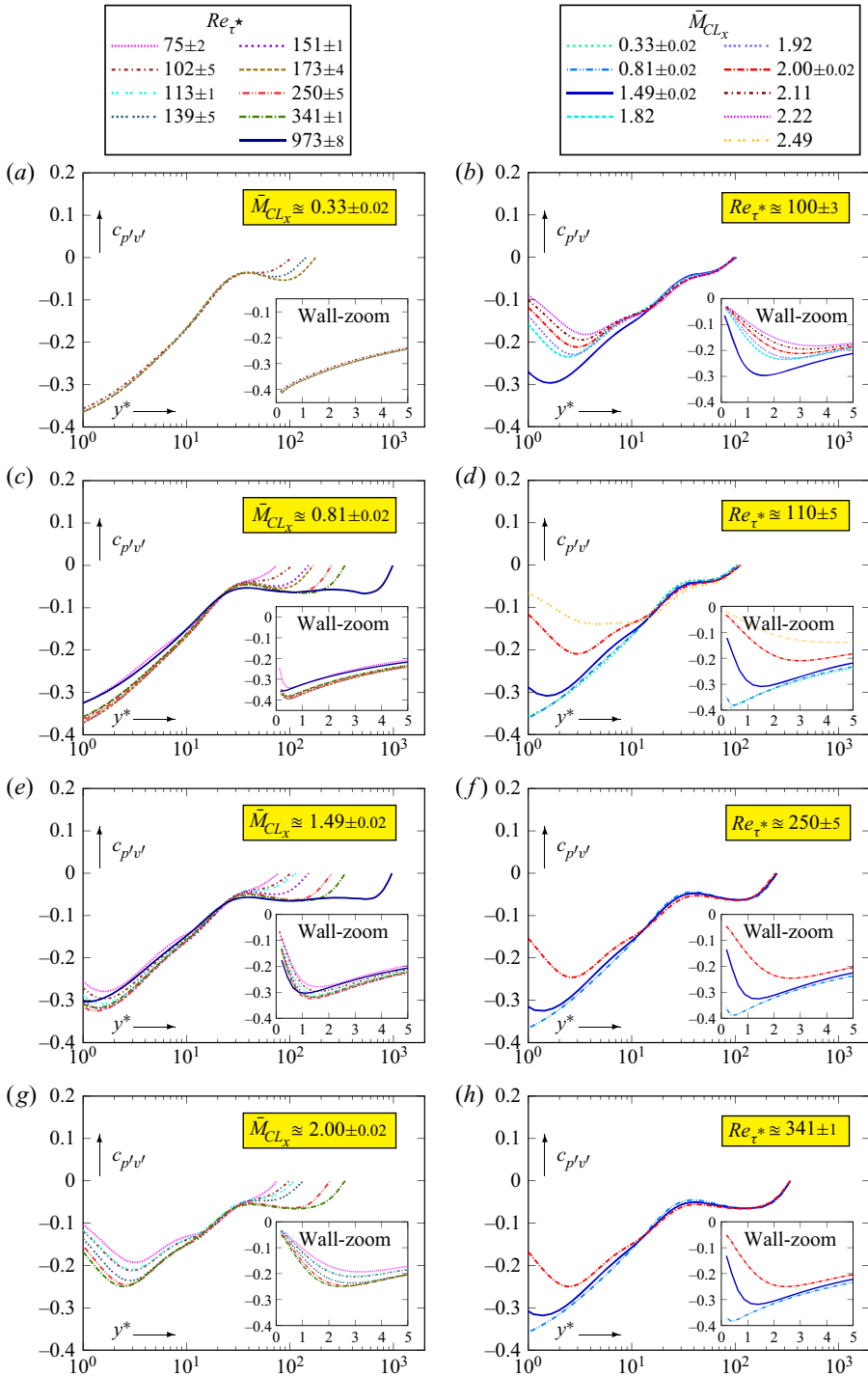


Figure 9. Profiles of correlation coefficient $c_{p'v'}$ of wall-normal pressure transport (3.4a,b), plotted against the HCB-scaled non-dimensional distance from the wall y^* (logscale and linear wall-zoom), for varying HCB Reynolds numbers $73 \leq Re_{\tau^*} \leq 983$ at constant centreline Mach-numbers $\bar{M}_{CLx} \in \{0.33, 0.80, 1.50, 2.00\}$, and for varying centreline Mach numbers $0.32 \leq \bar{M}_{CLx} \leq 2.49$ at constant HCB Reynolds numbers $Re_{\tau^*} \in \{100, 110, 250, 340\}$, from the present DNS database (table 1).

the positive correlation of p' with the streamwise velocity fluctuation u' near the wall (figure 8). This region ($y^* \lesssim 15$) corresponds precisely to the region where an increase of p'^+_{rms} was observed with increasing \bar{M}_{CL_x} (figure 3).

Regarding $c_{p'v'}$ (figure 9) we observe near the wall ($y^* \lesssim 15$) a very marked influence of \bar{M}_{CL_x} , at constant Re_{τ^*} , both in level and slope. For all of the $(Re_{\tau^*}, \bar{M}_{CL_x})$ flow conditions in the database (table 1) we have roughly $c_{p'v'}(y^* \approx y^*_{p'PEAK}) \approx -0.05$, which progressively develops to a plateau with increasing Re_{τ^*} . At low $\bar{M}_{CL_x} \approx 0.33$, $c_{p'v'}$ decreases monotonically for $y^* \lesssim y^*_{p'PEAK}$ towards the wall where it reaches a high negative value $-[c_{p'v'}]_w \approx 0.4$ (depending on Re_{τ^*}), in line with incompressible flow data (Hoyas & Jiménez 2006; Lee & Moser 2015). At the incompressible flow limit, which is quite well represented by the $\bar{M}_{CL_x} \approx 0.33$ data (Gerolymos *et al.* 2013; Gerolymos & Vallet 2016), the region $y^* \lesssim y^*_{p'PEAK}$ is dominated by (p', v') events of opposite sign (figure 9), the more so as the wall is approached. The data at $\bar{M}_{CL_x} \approx 0.8$ indicate similar behaviour, up to the deep viscous sublayer, where we observe a very slight decrease of the negative correlation $-c_{p'v'} = |c_{p'v'}|$, for $y^* \lesssim \frac{1}{2}$, at $Re_{\tau^*} \lesssim 340$ (figure 9). This decrease of $-c_{p'v'}$ with increasing \bar{M}_{CL_x} is an important trend, as confirmed by the data for $\bar{M}_{CL_x} \approx 1.5$ (figure 9), where it starts at $y^* \lesssim 1.5$ reaching wall-values of $-[c_{p'v'}]_w \lesssim 0.1$, nearly four times less than at $\bar{M}_{CL_x} \approx 0.33$. Note also that the $\bar{M}_{CL_x} \approx 1.5$ data at constant Re_{τ^*} deviate from the lower $\bar{M}_{CL_x} \approx 0.8$ data already at $y^* \lesssim 15$. For $\bar{M}_{CL_x} \approx 2$ this deviation is larger and the negative peak (NP) of $c_{p'v'}$ occurs at $y^* \approx 2.5$, with a very strong positive slope nearer to the wall, where near-zero values are observed (figure 9). This compressibility effect becomes more pronounced at higher \bar{M}_{CL_x} as shown by the $Re_{\tau^*} \approx 100$ data at progressively increasing $\bar{M}_{CL_x} \in \{1.5, 1.8, 1.9, 2.0, 2.1, 2.2\}$ (figure 9). For the case $(Re_{\tau^*}, \bar{M}_{CL_x}) = (113, 2.49)$ there is a monotonic increase of $c_{p'v'}$ towards $[c_{p'v'}]_w \lesssim 0$ in the entire region $y^* \lesssim 15$ (figure 9).

There is, nonetheless, a Re_{τ^*} -effect as well, the decrease of $-c_{p'v'}$ becoming weaker and occurring closer to the wall with increasing Re_{τ^*} (figure 9).

This substantial modification in the pressure–velocity correlations suggests a noticeable modification of the near-wall pressure field by compressibility. With increasing \bar{M}_{CL_x} , both the extent of the near-wall region impacted by the compressibility effects and the difference from the incompressible behaviour increase significantly (figures 8, 9). Note that the region $y^* \lesssim 10$ is also the region where both wall-echo effects and the Stokes term in the $\nabla^2 p'$ splitting are important (Gerolymos *et al.* 2013).

Regarding the outer part of the flow, note that $c_{p'v'}$ profiles (figure 9) have little \bar{M}_{CL_x} influence, whereas there is a weak \bar{M}_{CL_x} effect on $c_{p'u'}$ (figure 8).

4. Near-wall streaks and pressure field

To understand the physical mechanisms behind these near-wall effects we can use equations (e.g. for $\nabla^2 p'$ or for $D_t \overline{p'^2}$) and/or examine the coherent structures in this region. In the present paper, we concentrate on the coherent structures, in an effort to identify structural changes in the flow.

In the following, we present results at nearly constant $Re_{\tau^*} \approx 110$ for which the widest range $0.32 \leq \bar{M}_{CL_x} \leq 2.49$ is available (table 1). These are confirmed at higher $Re_{\tau^*} \in \{250, 340\}$ and lower $Re_{\tau^*} \approx 102$, which are not reported, for conciseness.

Note also that the $(Re_{\tau^*}, \bar{M}_{CL_x}) = (113, 2.49)$ flow (Gerolymos & Vallet 2014, 2018) corresponds to the same conditions as the flow analysed by Tang *et al.* (2020) to identify near-wall compressibility effects.

The previous analysis (§ 3) of p' variance and correlations highlights the important effects of varying \bar{M}_{CL_x} at constant Re_{τ^*} on the near-wall ($y^* \lesssim 15$) p' -field. This is in line with previous work (Yu *et al.* 2019; Tang *et al.* 2020), but the availability of the present $(Re_{\tau^*}, \bar{M}_{CL_x})$ -matrix database (table 1) allows us to evaluate the influence of each of the two parameters separately. Far more than the differences in p'_{rms} (figure 3), the large (with increasing \bar{M}_{CL_x}) modifications in the pressure–velocity correlation coefficients $c_{p'u'}$ and $c_{p'v'}$ near the wall (figures 8, 9) are structural modifications (Bradshaw 1977) suggesting significant differences in the flow field near the wall.

This region ($y^* \lesssim 15$) where p' -statistics are strongly \bar{M}_{CL_x} -dependent is precisely the region where flow structure and dynamics are dominated by the near-wall streaks (Chernyshenko & Baig 2005a,b; Wang, Pan & Wang 2019) characteristic of buffer-layer turbulence (Panton 2001; Adrian 2007; Bernard 2019), but which actually extend also into the viscous sublayer, practically down to the wall. As $y \rightarrow y_w$ approaching the wall

$$y^+ \rightarrow 0 \implies \begin{matrix} \bar{\rho}(y) \rightarrow \bar{\rho}_w \\ \bar{\mu}(y) \rightarrow \bar{\mu}_w \end{matrix} \xrightarrow{(2.1a), (2.1c)} \begin{matrix} x^* \rightarrow x^+ \\ y^* \rightarrow y^+ \\ z^* \rightarrow z^+ \end{matrix} . \quad (4.1)$$

Hence, for increasing \bar{M}_{CL_x} , because of the strong mean-temperature stratification (figure 1), the wall-normal gradient of the HCB length-unit $\partial_y \ell_{UNIT}^*$ becomes increasingly strong. Therefore, any near-wall phenomenon ($y^* \lesssim 15$) whose length scale is almost constant or slowly varying in the wall-normal direction cannot be correctly represented in HCB-scaled spatial coordinates.

It turns out that the spanwise distance between streaks is precisely such a flow feature. As we are interested in comparing flow fields near the wall, we need to determine what is the appropriate length-unit for $\{x, y, z\}$.

4.1. Scaling of the spanwise distance between streaks

A good surrogate for this distance in an average sense can be defined via the spanwise two-point correlation coefficient of the streamwise velocity (Chernyshenko & Baig 2005b)

$$C_{u'u'}^{(z)}(y, \xi_z) := \frac{\overline{u'(x, y, z, t) u'(x, y, z + \xi_z, t)}}{\overline{u'^2(y)}}, \quad (4.2a)$$

where the footprint of the streaks is the appearance of a strong (~ -0.2) negative peak (NP) before the correlation increases again towards 0 (figure 10). This NP is attributed to the negative correlation between low velocities ($u' < 0$) inside the streaks with the high velocities ($u' > 0$) in the adjoining region. It ‘may be used to assign a length scale to the turbulence’ (Tritton 1988, p. 307), namely, the distance of the first NP from the origin of ξ_z (4.2a)

$$A_{u'}^{(z; NP)} := \min |\xi_z| \left| \begin{matrix} \partial_{\xi_z} C_{u'u'}^{(z)}(y, \xi_z) = 0, \\ C_{u'u'}^{(z)}(y, \xi_z) < 0. \end{matrix} \right. \quad (4.2b)$$

Chernyshenko & Baig (2005b) suggest that twice this length scale is a good estimate for the average distance between streaks

$$\Lambda_S^{(z)} := 2\Lambda_{u'}^{(z;NP)}. \quad (4.2c)$$

Of course there are much more advanced techniques for identifying the streaks as coherent structures, either on each (xz) -plane (Wang *et al.* 2019) or as three-dimensional structures (Bernard 2019; Bae & Lee 2021), allowing a more accurate statistical determination of an average distance between streaks, but the surrogate (4.2c) is sufficient for the purposes of the present work.

Plotting the correlation coefficient $C_{u'u'}^{(z)}(y, \xi_z)$ (4.2a) against ξ_z^+ in standard wall-units (2.1a) at different wall-normal stations $y^* \in \{1, 5, 10, 15, 20\}$ (figure 10) clearly shows little variation with wall distance for given flow conditions $(Re_{\tau^*}, \bar{M}_{CL_x})$. As in standard wall-units, the length-unit does not depend on wall distance, this suggests that the spanwise spacing of the streaks, for given flow conditions $(Re_{\tau^*}, \bar{M}_{CL_x})$, varies little with y in the near-wall region ($y^* \gtrsim 15$). On the other hand, expectedly, standard wall-units (2.1a) scaling of ξ_z^+ shows very important differences with increasing \bar{M}_{CL_x} at nearly constant Re_{τ^*} , exactly analogous to the strong \bar{M}_{CL_x} -dependence of the ratio Re_{τ_w}/Re_{τ^*} (table 1).

Plotting the correlation coefficient $C_{u'u'}^{(z)}(y, \xi_z)$ (4.2a) against ξ_z^* in HCB-scaled units (2.1b) illustrates both the successes and shortcomings of this scaling. Sufficiently away from the wall ($y^* \approx 20$) the two-point correlation coefficients $C_{u'u'}^{(z)}$ for different \bar{M}_{CL_x} at nearly constant Re_{τ^*} practically collapse on a single curve when plotted against ξ_x^* (figure 10). However, closer to the wall, as progressively $y \rightarrow 0 \implies \xi_z^* \rightarrow \xi_z^+$ (4.1), the substantial differences between different \bar{M}_{CL_x} are recovered, e.g. at $C_{u'u'}^{(z)}(y^* \approx 1, \xi_z^+) \approx C_{u'u'}^{(z)}(y^* \approx 1, \xi_z^*)$ (figure 10).

This behaviour is better understood by considering the profiles (against y^*) of the distance between streaks (4.2c) in the two scalings, $\Lambda_S^{(z)+}$ and $\Lambda_S^{(z)*}$, in the entire buffer region (figure 11). Data at $Re_{\tau^*} \approx 110$ for different $\bar{M}_{CL_x} \in \{0.32, 0.79, 1.51, 2.02, 2.49\}$ show that the HCB-scaled $\Lambda_S^{(z)*}$ is not particularly sensitive to \bar{M}_{CL_x} for $y^* \gtrsim 15$, but also reveal increasingly large differences (with increasing \bar{M}_{CL_x}) when approaching the wall (figure 11), in line with (4.1). Note, in particular, how, for $(Re_{\tau^*}, \bar{M}_{CL_x}) = (113, 249)$, $\Lambda_S^{(z)*}(y^* \rightarrow 0)$ increases sharply towards values approaching $\Lambda_S^{(z)+}$ at the wall which are outside of the plot range (figure 11).

As we are interested in examining flow fields in the near-wall region, we need a length unit that does not vary in the wall-normal direction, to conform with the fact that in physical space the spanwise distance between streaks (which is a physically relevant length scale) varies little wall-normal-wise (figures 10, 11). On the other hand, this length-unit should approach ℓ_{UNIT}^* for $y^* \gtrsim 15$ where HCB scaling is successful in accounting for \bar{M}_{CL_x} effects. One possible, but rather difficult to use in practice, choice would be to use $\ell_{UNIT}^*(y)$ for all $y^* \geq y_{p'PEAK}^*$, and use a constant $\ell_{UNIT}^*(y_{p'PEAK}^*)$ for all $y^* \leq y_{p'PEAK}^*$ from the p'_{rms} peak (3.2) down to the wall. However, this complexity is not necessary. The y -dependence of $\ell_{UNIT}^*(y)$ (2.1b) stems essentially from the mean-temperature stratification of the flow (figure 1) which induces the variations of $\bar{\mu}(y)$ and $\bar{\rho}(y)$ (§ 2.1). Closer observation of the $\tilde{T}(y)$ profiles (figure 1) reveals that strong temperature variations actually occur only in the near-wall region ($y^* \lesssim 20$), for a given $(Re_{\tau^*}, \bar{M}_{CL_x})$

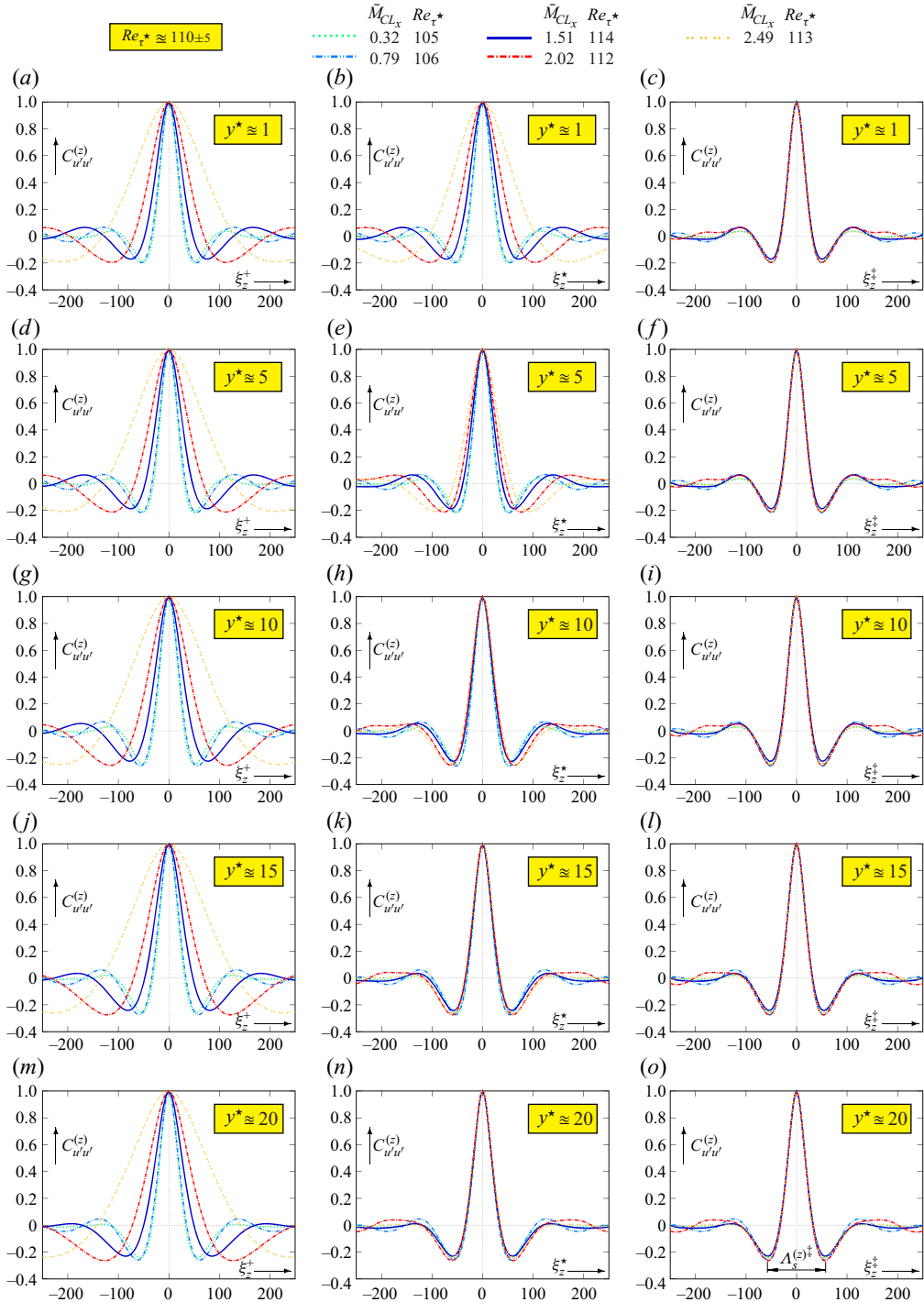


Figure 10. Two-point spanwise correlation coefficient of streamwise velocity fluctuations $C_{u'u'}^{(z)}(y; \xi_z)$ (4.2a), at different HCB-scaled non-dimensional distances from the wall $y^* \in \{1, 5, 10, 15, 20\}$, plotted against different non-dimensionalisations (2.1) of the distance between the two points $\{\xi_z^+, \xi_z^*, \xi_z^{\ddagger}\}$, for varying centreline Mach numbers $0.32 \leq \bar{M}_{CL_x} \leq 2.49$ at nearly constant $Re_{\tau}^* \approx 110$ (table 2); the average distance between streaks surrogate $A_S^{(z)\ddagger}$ (4.2b), (4.2c) is indicated at $y^* \approx 20$.

Pressure fluctuations in compressible wall turbulence

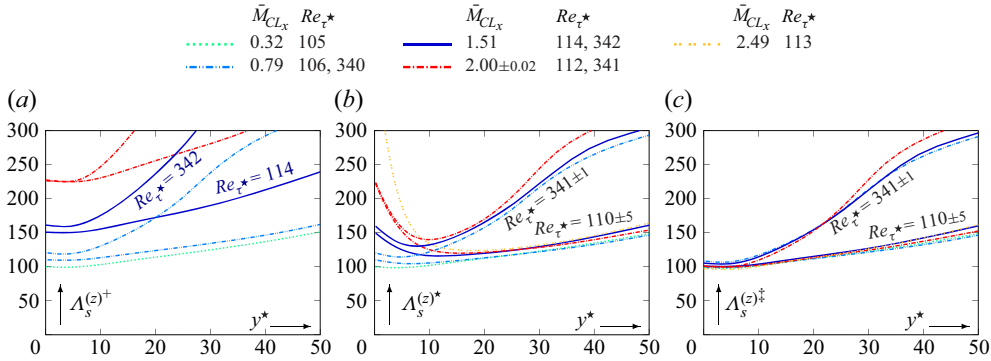


Figure 11. Different non-dimensionalisations (2.1) $\{\Lambda_S^{(z)+}, \Lambda_S^{(z)*}, \Lambda_S^{(z)\ddagger}\}$ of the surrogate for the average spanwise distance (4.2b), (4.2c), plotted against the HCB-scaled non-dimensional distance from the wall y^* (2.1b), at nearly constant $Re_{\tau^*} \in \{110 \pm 5, 341 \pm 1\}$ for different $\bar{M}_{CL_x} \in \{0.32, 0.79, 1.51, 2.00 \pm 0.02, 2.49\}$ (table 2); enlarged view of the region $y^* \leq 50$.

flow, whereas in the outer region ($y^* \gtrsim 20$) temperature variations are much smaller ($\tilde{T}_{CL} - \tilde{T}(y) \ll \tilde{T}_{CL} - \tilde{T}_w \forall y^* \gtrsim 20$). Therefore, a system of units based on $\bar{\tau}_w$, which was found to be an appropriate scale for p' (§ 3), and centreline thermodynamic quantities $\{\bar{\rho}_{CL}, \bar{\mu}_{CL}\}$ should be very close to $(\cdot)^*$ units for $y^* \gtrsim 15$, while being y -independent. For TPC flow (2.2b), these are precisely the $(\cdot)^\ddagger$ units (2.1c) introduced in § 2.1, which retain with a very good accuracy the advantages of the HCB scaling in the outer part of the flow, while respecting the very small y variation of the (xz) organisation of the flow very near the wall. Furthermore, in TPC flow, this system of units also maintains $Re_{\tau^*} = Re_{\tau^\ddagger}$ (2.2a) as the relevant Reynolds number.

Plotting the correlation coefficient $C_{u'u'}^{(z)}(y, \xi_z)$ (4.2a) against ξ_z^\ddagger practically collapses the curves for the different $\bar{M}_{CL_x} \in \{1.51, 2.02, 2.49\}$ at $Re_{\tau^*} \approx 110$, for all $y^* \in \{1, 5, 10, 15, 20\}$ (figure 10). The applicability of the $(\cdot)^\ddagger$ units (2.1c) is further confirmed by the profiles of $\Lambda_S^{(z)\ddagger}(y)$ (figure 11) which are clustered closely together for the different $\bar{M}_{CL_x} \in \{0.32, 0.79, 1.51, 2.00 \pm 0.02, 2.49\}$ at $Re_{\tau^*} \approx 110$. These profiles of $\Lambda_S^{(z)\ddagger}(y)$ are very similar with those obtained in incompressible flow (Chernyshenko & Baig 2005b, figure 1, p. 1100).

The scaling of the streamwise two-point correlation

$$C_{u'u'}^{(x)}(y, \xi_x) := \frac{\overline{u'(x, y, z, t) u'(x + \xi_x, y, z, t)}}{u'^2(y)} \quad (4.2d)$$

with ξ_x^\ddagger (2.1c) is also quite satisfactory, compared with ξ_x^+ (2.1a) or ξ_x^* (2.1b), in that it very efficiently clusters together the curves for different \bar{M}_{CL_x} at nearly constant Re_{τ^*} (figure 10). Nonetheless, there remains, expectedly, a small \bar{M}_{CL_x} -dependence which slightly increases as y decreases towards the wall (figure 10). This observation highlights the fact that both $(\cdot)^*$ units (2.1b) and $(\cdot)^\ddagger$ units (2.1c) may show \bar{M}_{CL_x} -dependence very near the wall, but the latter are less \bar{M}_{CL_x} -sensitive and have the advantage of being y -independent and of not tending to $(\cdot)^+$ units (2.1a) at the wall.

4.2. Appearance of organised pressure waves with increasing \bar{M}_{CL_x}

The low-speed streaks in the near-wall region can be identified (figure 13) using the conditional average (truncated distribution)

$$\overline{M_x | M'_x < 0} := \frac{\int_{M_{x_{min}}}^{\bar{M}_x} M_x f_{M_x}(M_x) dM_x}{\int_{M_{x_{min}}}^{\bar{M}_x} f_{M_x}(M_x) dM_x}, \tag{4.3}$$

where $M_{x_{min}}$ is the minimum observed M_x and f_{M_x} the corresponding p.d.f. This simple parameter-free choice (only requiring sampling the p.d.f. of M_x) performs quite well (figure 13), thus avoiding user-defined thresholds (Wang *et al.* 2019) or percolation techniques (Bae & Lee 2021). Note that the spanwise distance between the instantaneous streaks in the (x^\ddagger, z^\ddagger) -plane (figure 13) varies little with \bar{M}_{CL_x} , in line with the previous analysis (§ 4.1) which resulted in the introduction of $(\cdot)^\ddagger$ units (2.1c).

It is not easy to identify structures by simply visualising instantaneous p' -fields (figure 14). For the higher $\bar{M}_{CL_x} = 2.49$ case, the $(+/-)$ - p' regions, which were identified and analysed for the same flow conditions by Tang *et al.* (2020), are visible inside the streaks (figure 14). Note also that we can sometimes discern bow-like $(+/-)$ - p' regions connecting corresponding regions between neighbouring streaks. At $\bar{M}_{CL_x} = 2.02$ the same pattern is observed (figure 14), but with lower spatial density (probability of occurrence), and at lower $\bar{M}_{CL_x} = 1.51$, $(+/-)$ - p' regions are visible essentially at the boundaries of the streaks, with much less and weaker streamwise events or connecting bow structures (figure 14).

To better identify the p' -structures it is preferable to use gradients or Laplacians similarly to standard optical visualisation techniques (Liepmann & Roshko 1957, pp. 157–163). After testing different options it appeared that the in-plane Laplacian

$$\nabla_{xz}^2 p' := \frac{\partial^2 p'}{\partial x^2} + \frac{\partial^2 p'}{\partial z^2} \tag{4.4}$$

is a very good choice. Note that for the present xz -invariant-in-the-mean flow, $\nabla_{xz}^2 p' = \nabla_{xz}^2 p$, so that (4.4) can be evaluated without the knowledge of $\bar{p}(y)$. Furthermore, $\nabla_{xz}^2 p'$ only requires in-plane data which allows y -subsampling in data extraction. Following the previous analysis (§ 4.1) of the two-point correlation coefficients $C_{u'u'}^{(z)}(z; \xi_z)$ (figure 10) and $C_{u'u'}^{(x)}(y; \xi_x)$ (figure 12), and of the surrogate distance between streaks $\Lambda_S^{(z)\ddagger}(y)$ (figure 11), we used $(\cdot)^\ddagger$ units (2.1c) to non-dimensionalise $(\nabla_{xz}^2 p')^\ddagger$. Recall that the unit for p is $\bar{\tau}_w$ in all systems (2.3).

By analogy with harmonic waves, we may identify very approximately the high negative values of $(\nabla_{xz}^2 p')^\ddagger$ with p' -maxima and the high positive values with p' -minima. The wavefronts can actually be identified to the contours corresponding to $(\nabla_{xz}^2 p')^\ddagger = 0$ which separate the $(+/-)$ - p' regions. The waves, which are very clearly visible for the higher $\bar{M}_{CL_x} \in \{2.02, 2.49\}$ (figure 15), are essentially in the streamwise direction (x -wise), but the fronts (essentially z -wise for x -wise waves) seem to be faster in the high- M_x regions between streaks and slower within the low- M_x streaks, taking a bow shape in the high- M_x regions. More importantly, these bow fronts cross the streaks and seem to have spanwise

Pressure fluctuations in compressible wall turbulence

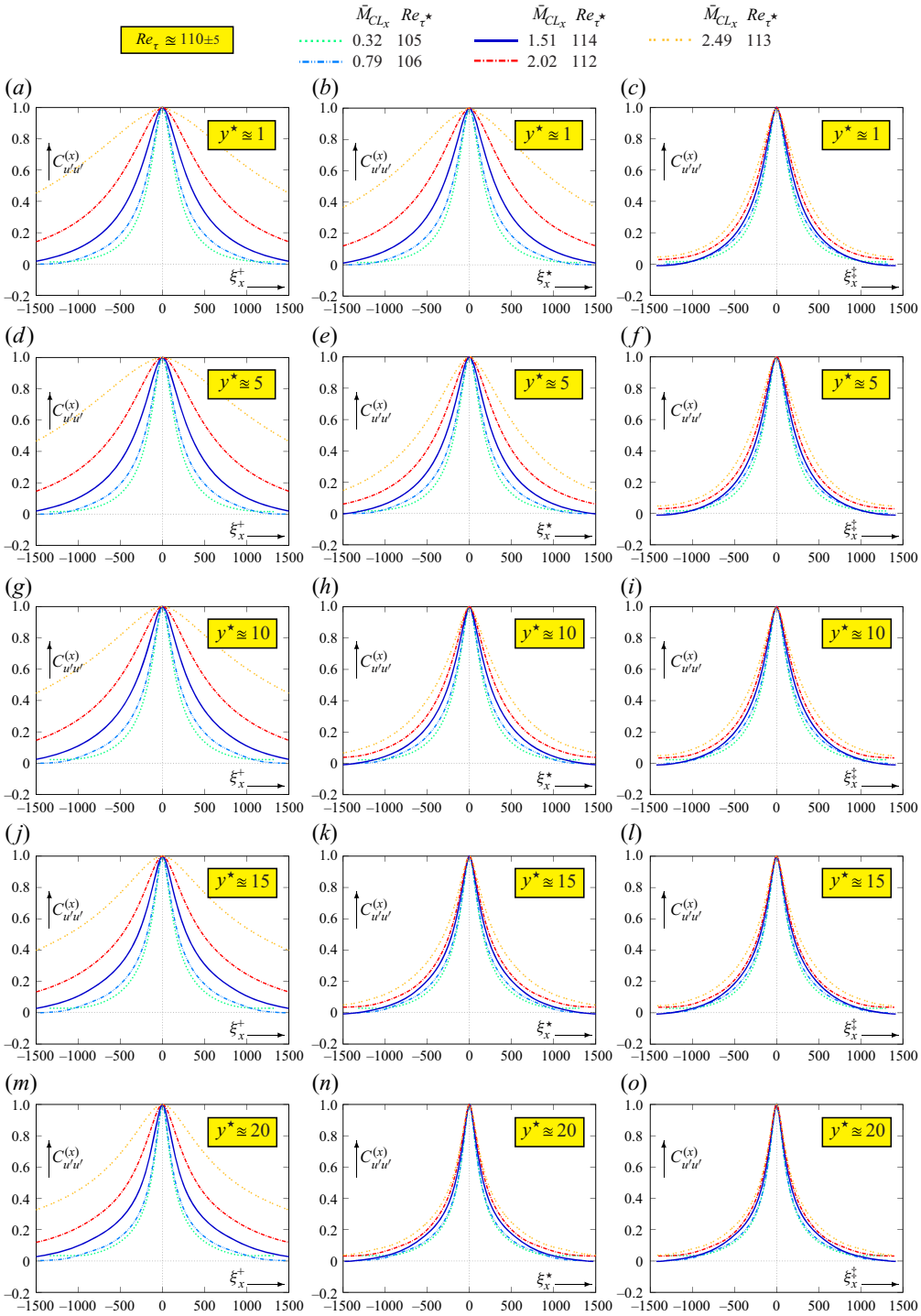


Figure 12. Two-point streamwise correlation coefficient of streamwise velocity fluctuations $C_{u'u'}^{(x)}(y; \xi_x)$ (4.2d), at different HCB-scaled non-dimensional distances from the wall $y^* \in \{1, 5, 10, 15, 20\}$, plotted against different non-dimensionalisations (2.1) of the distance between the two points $\{\xi_x^+, \xi_x^*, \xi_x^\ddagger\}$, for varying centreline Mach numbers $0.32 \leq \bar{M}_{CLx} \leq 2.49$ at nearly constant $Re_{\tau}^* \approx 110$ (table 2).

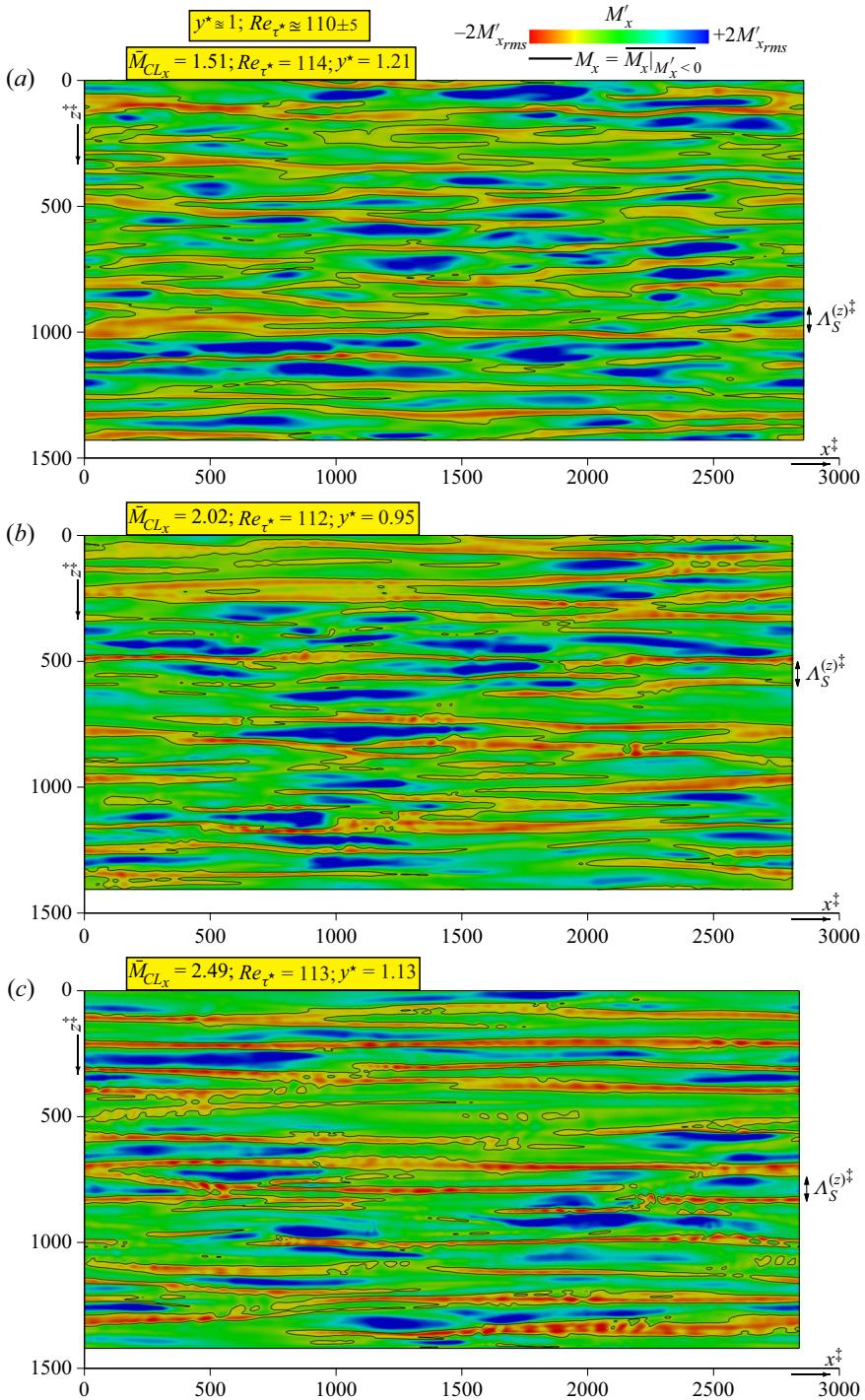


Figure 13. Instantaneous fluctuating streamwise Mach number M'_x (colourmap $-2M'_{x,rms} \leq M'_x \leq +2M'_{x,rms}$), on (x^\ddagger, z^\ddagger) planes very near the wall ($y^* \approx 1$), for different $\bar{M}_{CLx} \in \{1.51, 2.02, 2.49\}$ at nearly constant $Re_{\tau^*} \approx 110$ and approximate streak boundaries (black contours $M_x = \overline{M_x} |M'_x| < 0$); also included is the surrogate of the average spanwise distance between streaks $\Lambda_S^{(z)\ddagger}$ (4.2b), (4.2c).

Pressure fluctuations in compressible wall turbulence

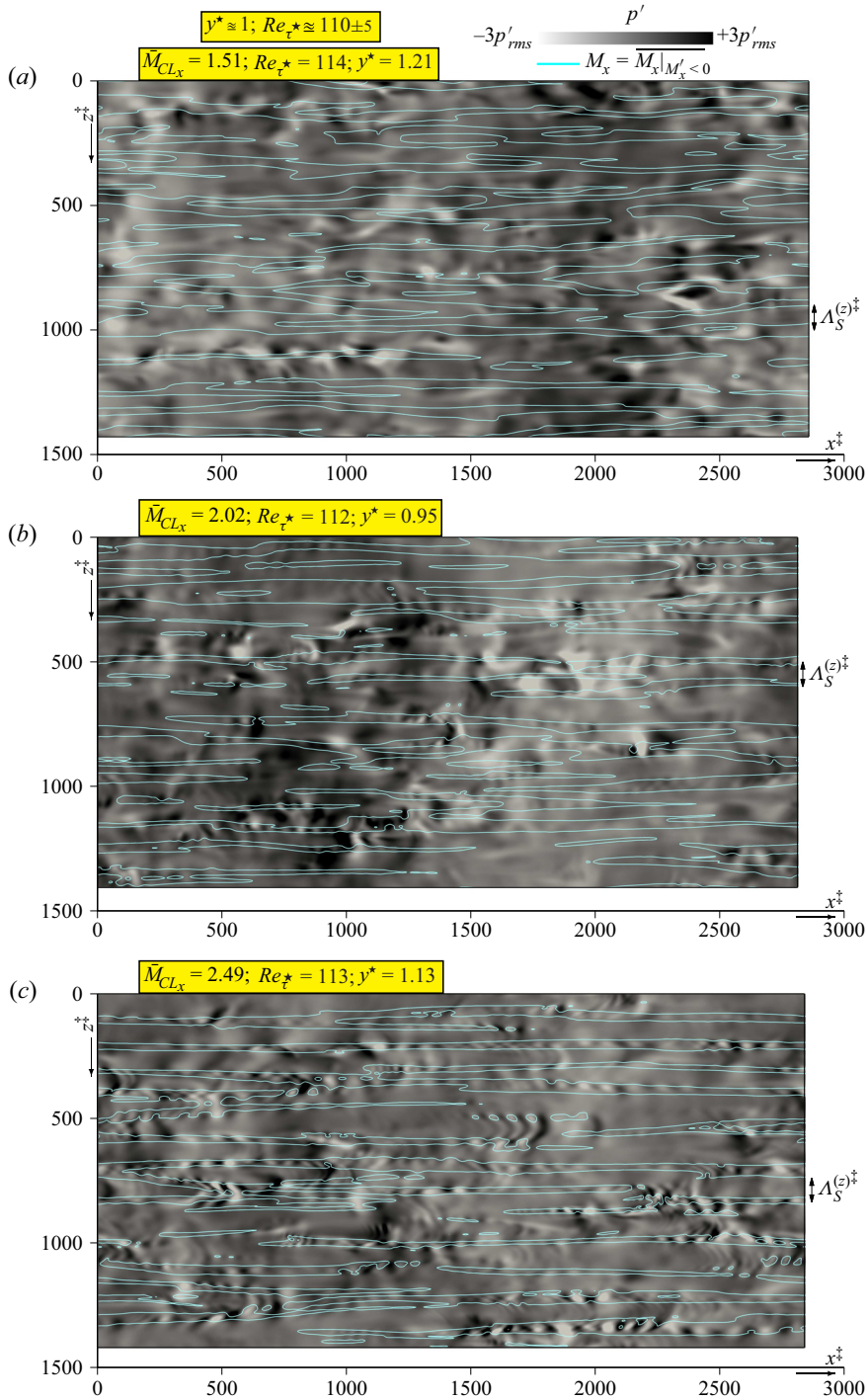


Figure 14. Instantaneous fluctuating pressure field p' (X-ray colourmap $-3p'_{rms} \leq p' \leq +3p'_{rms}$), on (x^\ddagger, z^\ddagger) planes very near the wall ($y^* \approx 1$), for different $\bar{M}_{CLx} \in \{1.51, 2.02, 2.49\}$ at nearly constant $Re_{\tau^*} \approx 110$ and approximate streak boundaries (cyan contours $M_x = \bar{M}_x|_{M'_x < 0}$); also included is the surrogate of the average spanwise distance between streaks $\Lambda_S^{(z)^\ddagger}$ (4.2b), (4.2c).

extent over several streaks (figure 15). A more detailed time-dependent analysis would be necessary to identify precisely the nature and statistics of these coherent structures, but this is beyond the scope of the paper and should be the subject of future research. It does seem plausible however that these cross-streak p' bow waves are related with the previously observed effects of \bar{M}_{CL_x} on p' -statistics and correlations with the velocity field near the wall.

Note that these bow waves are precisely connected to the $(+/-)p'$ structures inside the streaks (figure 14) which were identified and analysed by Tang *et al.* (2020). However, using $(\nabla_{xz}^2 p')^\ddagger$ has definite advantages in identifying the spanwise extent and spanwise coherence of these p' -waves, which is not as obvious by simply considering p' X-rays (figure 14) or p' -level plots (Tang *et al.* 2020). The $(+/-)p'$ regions inside the streaks are possibly the effect of the interaction of these pressure waves with the three-dimensional vortical structures responsible for the appearance of the streaks. In three dimensions the streaks are identified by pairs of counter-rotating structures of wall-normal vorticity ω_y which induce highly negative $u' < 0$ in the centre region of the streaks (Adrian 2007; Bernard 2019). Therefore the spanwise cross-streak coherence of the bow waves observed by studying $(\nabla_{xz}^2 p')^\ddagger$ (figure 15) is a feature of the near-wall p' field which requires further study. Note that with the hindsight of the detection of the wavefronts using $(\nabla_{xz}^2 p')^\ddagger$ (figure 15), the spanwise persistence of the waves between streaks is observable in the p' -field as well, especially with increasing \bar{M}_{CL_x} (figure 14).

These waves are essentially present in the near-wall region ($y^* \lesssim 15$), and have substantial amplitude with increasing \bar{M}_{CL_x} , so at the higher $\bar{M}_{CL_x} \in \{2.02, 2.49\}$ they are the dominant feature in the $(\nabla_{xz}^2 p')^\ddagger$ X-rays (figure 15). At $\bar{M}_{CL_x} = 1.51$ they no longer dominate the very-near-wall p' -field (figure 15), although a few weak streamwise events (spanwise fronts) are discernible. However, the fronts between $(+/-)p'$ regions have become mostly parallel to the streaks, implying that with decreasing \bar{M}_{CL_x} the amplitude of streamwise waves decreases, so that they no longer dominate the background p' -field at the wall, which becomes essentially associated with (induced by) the vortical structures responsible for the streaks. This is also the case at lower $\bar{M}_{CL_x} \in \{0.32, 0.79\}$. Although not shown, for conciseness, $(\nabla_{xz}^2 p')^\ddagger$ X-rays at different distances from the wall $y^* \in \{3, 5, 10, 15, 20, y_{p'PEAK}^*\}$ indicate that the density and intensity of the cross-streak streamwise bow waves, at constant high $\bar{M}_{CL_x} \in \{2.02, 2.49\}$ diminishes with increasing distance from the wall, and at $y^* \approx 20$ they are hardly discernible even for the highest $\bar{M}_{CL_x} = 2.49$. It is therefore plausible to associate this major modification of the p' -field, which is strengthened with increasing M_{CL_x} and with decreasing distance from the wall, to near-wall compressibility effects, precisely in the region where differences were observed in p'_{rms} (figure 3) and in the correlation coefficients $\{c_{p'u'}, c_{p'v'}\}$ (figures 8 and 9).

4.3. Pressure–velocity correlations near the wall

With the hindsight of the results above (§ 4.2) regarding the effect of \bar{M}_{CL_x} on the near-wall p' -field we reexamine the pressure–velocity correlations $c_{p'u'}$ and $c_{p'v'}$ (figures 8 and 9), by studying (figure 16) the integrands in the evaluation of $\{c_{p'u'}, c_{p'v'}\}$ (3.4a,b) from the

Pressure fluctuations in compressible wall turbulence

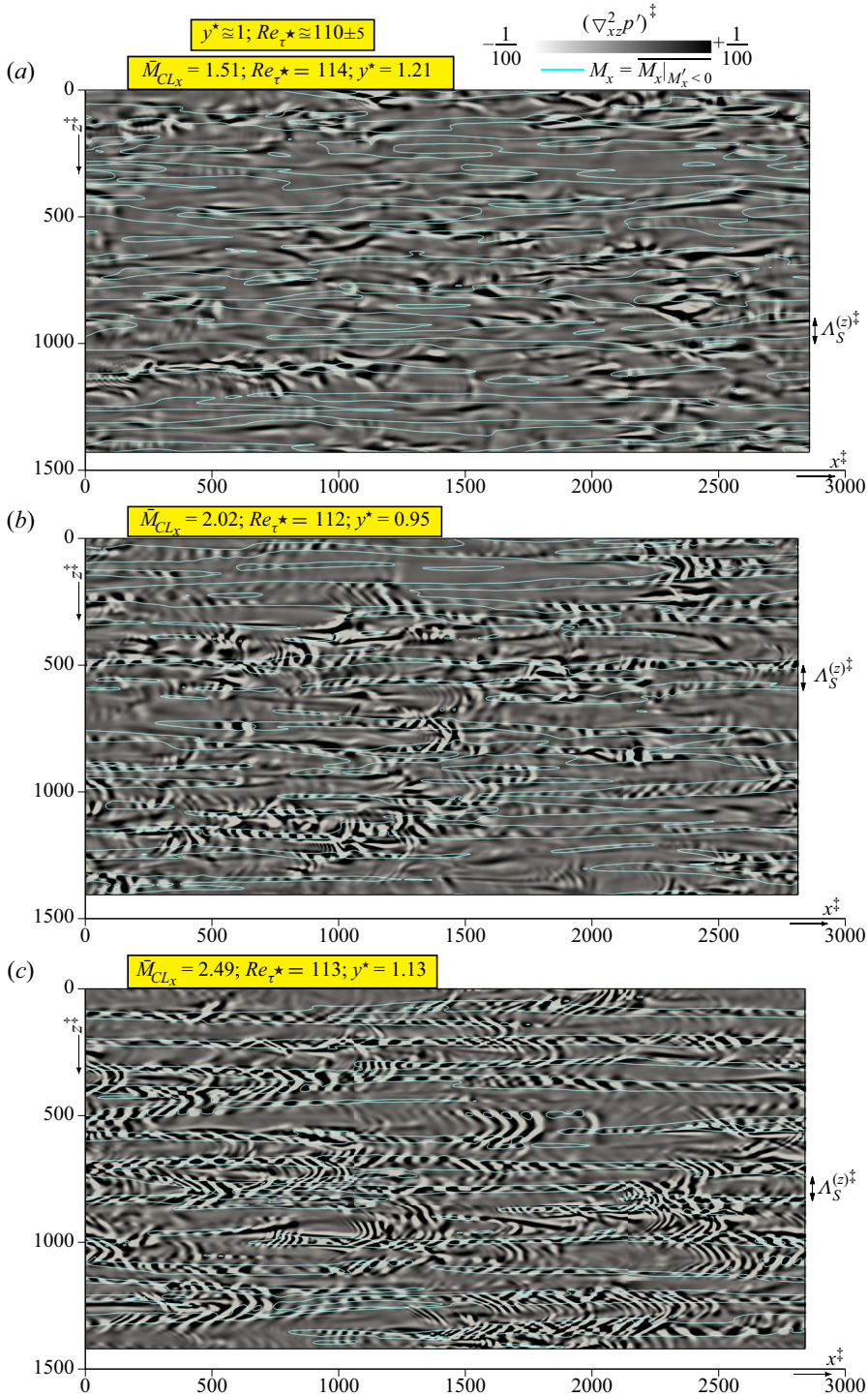


Figure 15. Instantaneous in-plane Laplacian of fluctuating pressure in mixed inner/outer scaling (2.1c) $(\nabla_{xz}p')^{\ddagger}$ (X-ray colourmap $-\frac{1}{100} \leq (\nabla_{xz}p')^{\ddagger} \leq +\frac{1}{100}$), on $(x^{\ddagger}, z^{\ddagger})$ planes very near the wall ($y^* \approx 1$), for different $\bar{M}_{CLx} \in \{1.51, 2.02, 2.49\}$ at nearly constant $Re_{\tau^*} \approx 110$ and approximate streak boundaries (cyan contours $M_x = \overline{M_x}|_{M'_x < 0}$); also included is the surrogate of the average spanwise distance between streaks $\Delta_S^{(z)\ddagger}$ (4.2b), (4.2c).

Re_{τ^*}	\bar{M}_{CL_x}	P.d.f.s; $\Delta t_{s_q} = \Delta t$			Joint p.d.f.s; $\Delta t_{s_{2q}} = \Delta t$			Two-point	
		$t_{OBS_q}^+$	N_{bins_q}	N_{s_q}	$t_{OBS_{2q}}^+$	$N_{bins_{2q}}$	$N_{s_{2q}}$	$\Delta t_{s_{R2}}$	$t_{OBS_{R2}}^+$
105	0.32	6531	200	251×10^9	3235	200×200	126×10^9	$10\Delta t$	1702
106	0.79	6828	200	97×10^9	4081	200×200	57×10^9	$10\Delta t$	1719
114	1.51	8014	200	103×10^9	4996	200×200	64×10^9	$10\Delta t$	1773
112	2.02	5098	200	291×10^9	3889	200×200	222×10^9	$10\Delta t$	1735
113	2.49	5166	1000	2245×10^9	5166	200×200	2243×10^9	$10\Delta t$	1659
340	0.80	5766	200	539×10^9	4483	200×200	419×10^9	$30\Delta t$	1762
342	1.51	5383	200	952×10^9	4048	200×200	715×10^9	$30\Delta t$	1663
341	1.98	3854	1000	2452×10^9	3854	200×200	2452×10^9	$50\Delta t$	1645

Table 2. Sampling parameters for p.d.f.s, joint p.d.f.s and two-point correlations: Re_{τ^*} is the friction Reynolds number in HCB-scaling (2.1b); \bar{M}_{CL_x} is the centreline Mach number (2.4); Δt is the computational time step (table 1); Δt_{s_q} , $\Delta t_{s_{2q}}$, $\Delta t_{s_{R2}}$ are the sampling time steps for p.d.f.s, joint p.d.f.s and two-point correlations; $t_{OBS_q}^+$, $t_{OBS_{2q}}^+$, $t_{OBS_{R2}}^+$ are the sampling observation intervals for p.d.f.s, joint p.d.f.s and two-point correlations; N_{bins_q} , $N_{bins_{2q}}$ are the sampling bins for the calculation of p.d.f.s and joint p.d.f.s; N_{s_q} , $N_{s_{2q}}$ is the number of samples involved in the calculation of p.d.f.s and joint p.d.f.s; $(\cdot)^+$ denotes wall-units (2.1a).

joint p.d.f.s $\{f_{p'u'}f_{p'v'}\}$ (table 2)

$$c_{p'u'} \stackrel{(3.4a,b)}{=} \int_{p'_{min}}^{p'_{max}} \int_{u'_{min}}^{u'_{max}} p'u' f_{p'u'}(p', u') d\left(\frac{p'}{p'_{rms}}\right) d\left(\frac{u'}{u'_{rms}}\right), \quad (4.5a)$$

$$c_{p'v'} \stackrel{(3.4a,b)}{=} \int_{p'_{min}}^{p'_{max}} \int_{v'_{min}}^{v'_{max}} p'v' f_{p'v'}(p', v') d\left(\frac{p'}{p'_{rms}}\right) d\left(\frac{v'}{v'_{rms}}\right), \quad (4.5b)$$

integrated with respect to the standardised variables

$$p'_{STD} := p'/p'_{rms}; \quad u'_{STD} := u'/u'_{rms}; \quad v'_{STD} := v'/v'_{rms}. \quad (4.5c)$$

Near the wall, the streamwise correlation $c_{p'u'}$ (figure 16) is dominated by $u' < 0$ events, essentially inside the streaks. The positive/negative correlation peaks occur at $u' \approx -u'_{rms}$ (figure 16), which is located approximately on or inside the streaks boundaries determined by $M_x = \bar{M}_x|_{M'_x < 0}$. At the lower $\bar{M}_{CL_x} \in \{0.32, 0.79, 1.51\}$ the integral of the positive $p'u' > 0$ quadrant Q_3 ($u'_{STD} < 0 > p'_{STD}$) is slightly higher than the integral of the negative $p'u' < 0$ quadrant Q_4 ($u'_{STD} < 0 < p'_{STD}$). With increasing \bar{M}_{CL_x} , the Q_3 contribution increases with respect to Q_4 , enhanced by $p' < 0$ events well inside the streaks ($u'_{STD} < -1 > p'_{STD}$). These statistical results suggest that the increase of $c_{p'u'}$ with increasing \bar{M}_{CL_x} in the near-wall region (figure 8) is probably the result of the interaction of the cross-streak pressure waves with the vortical structures inside the streaks, with little contribution from the high-speed regions between streaks.

Regarding the wall-normal correlation $c_{p'v'}$, the effect of \bar{M}_{CL_x} is more pronounced (figure 16), confirming that the decrease towards 0 of $-c_{p'v'} > 0$ with increasing \bar{M}_{CL_x} in the near-wall region (figure 9) is the result of structural changes in the flow. The positive $p'v' > 0$ quadrants Q_1 ($v'_{STD} > 0 < p'_{STD}$) and Q_3 ($v'_{STD} < 0 > p'_{STD}$) are nearly symmetric around the origin. With increasing \bar{M}_{CL_x} their weight increases relative to the negative quadrants Q_2 ($v'_{STD} > 0 > p'_{STD}$) and Q_4 ($v'_{STD} < 0 < p'_{STD}$), so that at the higher

Pressure fluctuations in compressible wall turbulence

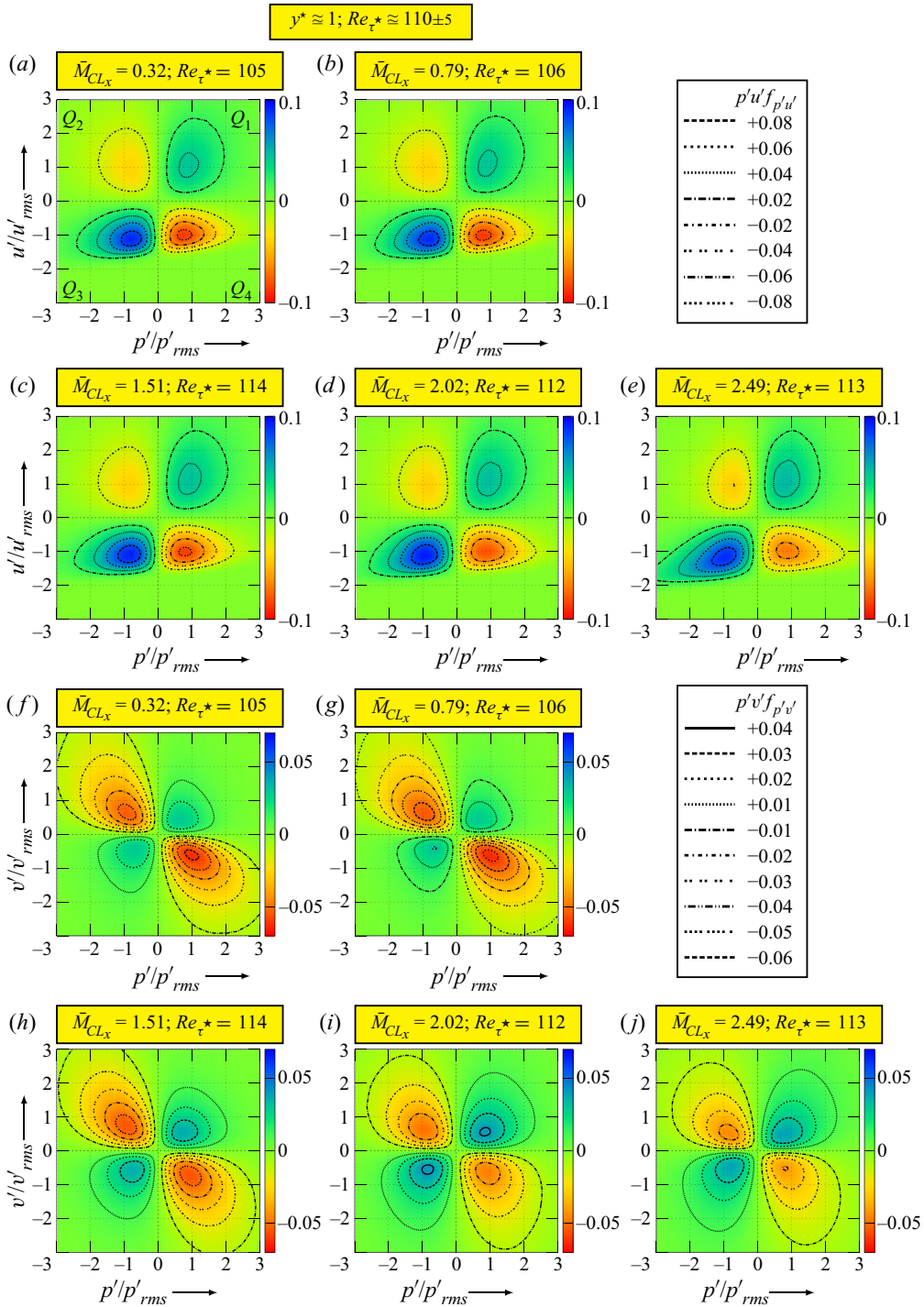


Figure 16. Integrands in the calculation of the correlation coefficients $c_{p'u'}$ (4.5a) and $c_{p'v'}$ (4.5b) from the corresponding joint p.d.f.s, plotted against the standardised variables $\{p'/p'_{rms}, u'/u'_{rms}, v'/v'_{rms}\}$, very near the wall ($y^* \approx 1$), at nearly constant $Re_{\tau}^* \approx 110$ for different $\bar{M}_{CLx} \in \{0.32, 0.79, 1.51, 2.02, 2.49\}$.

$\bar{M}_{CL_x} \in \{2.02, 2.49\}$ the integral approaches 0. This is in complete contrast with the lower $\bar{M}_{CL_x} \in \{0.32, 0.79, 1.51\}$ where the negative quadrants are clearly dominant (figure 16), the more so with decreasing \bar{M}_{CL_x} , with the maximum of Q_4 ($v'_{STD} < 0 < p'_{STD}$) being higher than that of Q_2 ($v'_{STD} > 0 > p'_{STD}$). Note also that there are increasing contributions from the positive quadrants (Q_1 and Q_3) with increasing \bar{M}_{CL_x} . At the higher $\bar{M}_{CL_x} = 2.49$ the integrands of $c_{p'v'}$ have become practically antisymmetric with respect to the zero axes (figure 16), explaining by cancellation the very low value of $-c_{p'v'}$ (figure 9).

The instantaneous contours $\nabla_{xz}^2 p' = 0$ are also the boundaries (fronts) between $(+/-) - p'$ events, whereas the instantaneous contours $M_x = \overline{M_x | M'_x < 0}$ highlight the low- u streaks (generally the statistics of M_x and u are very similar). The correlation of this $\{p', u'\}$ -fields organisation with the wall-normal velocity v' can be visualised by superposing the instantaneous p' -fronts and the low-speed streaks boundaries with the instantaneous M'_y -field (figure 17). At the higher $M_{CL_x} = 2.49$, high-intensity $(+/-) - M'_y$ events occur invariably on the p' -fronts ($\nabla_{xz}^2 p' = 0$ contours), and have precisely the same spanwise coherence and organization as the cross-streak p' -bow-waves (figure 17). At $\bar{M}_{CL_x} = 2.02$, in the regions where cross-streak p' -bow-fronts are present, the $(+/-) - M'_y$ events coincide with the fronts (figure 17). However, in the regions where the p' -fronts have started to align themselves with the streaks the $(+/-) - M'_y$ events appear elongated in the streamwise direction, and no longer coincide with the location of the fronts (figure 17). At $M_{CL_x} = 1.51$, the majority of p' -fronts are aligned with the streamwise direction, and $(+/-) - M'_y$ events are elongated in the streamwise direction and no longer coincide with the p' -fronts (figure 17).

Explaining the \bar{M}_{CL_x} -induced structural modifications of the wall-normal correlation $c_{p'v'}$ is obviously more complicated than for the streamwise correlation $c_{p'u'}$. The strong negative $c_{p'v'}$ correlation coefficients observed at low \bar{M}_{CL_x} can be associated to $(+/-) - v'$ events that form relatively elongated streamwise structures which do not coincide with the p' -fronts, as, e.g., in the $\bar{M}_{CL_x} = 1.51$ case (figure 17). At higher $\bar{M}_{CL_x} = 2.49$ the flow structure is completely masked by high-intensity $(+/-) - v'$ events which coincide with the fronts of the cross-streak bow-waves (figure 17), and which symmetrise the $c_{p'v'}$ -integrand (figure 16). It is not clear whether it is possible to analyse this modification as an additive compressible effect, via linear approaches (Tang *et al.* 2020), or if there are important nonlinear effects (Chu & Kovásznyai 1958) that become dominant with increasing \bar{M}_{CL_x} .

5. Conclusions

The construction of the $(Re_{\tau^*}, \bar{M}_{CL_x})$ -matrix DNS database of compressible TPC flow presented in this paper enables the precise evaluation of the effect of each of the two flow-determining parameters, the other being held constant. The present study focusses on the effects of these two parameters on the fluctuating pressure p' . The wall-to-recovery temperature ratio \bar{T}_w/T_r is not a free parameter, but is the result of viscous heating determined by $(Re_{\tau^*}, \bar{M}_{CL_x})$. Therefore, results in the paper correspond to increasingly cold-wall conditions (relative to adiabatic-wall temperature) with increasing \bar{M}_{CL_x} .

The average wall shear stress $\bar{\tau}_w$ is a very satisfactory scale for the level of pressure fluctuations, $p'_{rms}^+ \equiv p'^*_{rms}$ (identical in $(\cdot)^+$ wall-units or $(\cdot)^*$ HCB units), which is much more sensitive on Re_{τ^*} than on \bar{M}_{CL_x} . The strongest compressibility effects on p'_{rms} appear

Pressure fluctuations in compressible wall turbulence

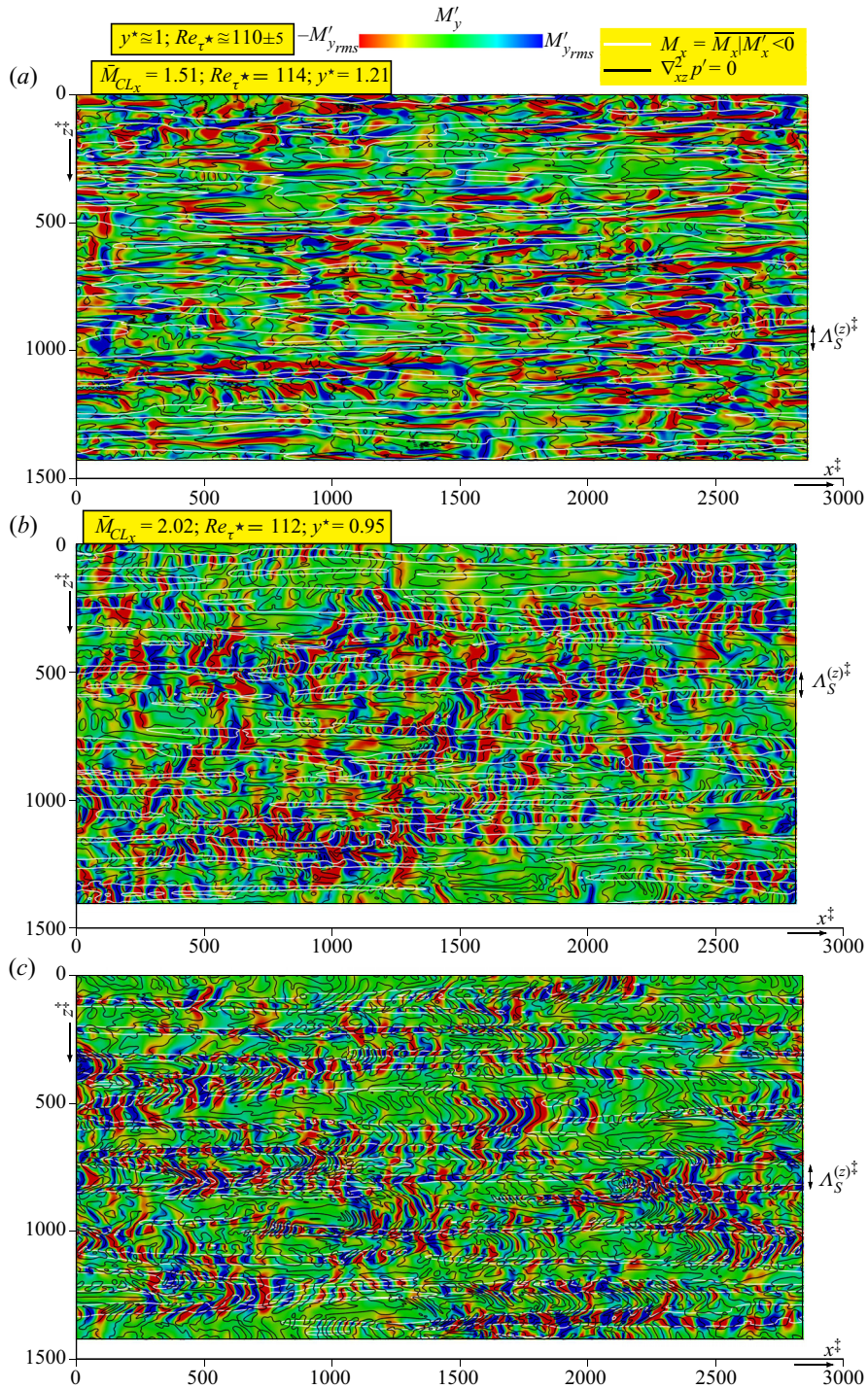


Figure 17. Instantaneous wall-normal Mach number fluctuation M'_y (colourmap $-M'_{y,rms} \leq M'_y \leq +M'_{y,rms}$), on $(x^{\ddagger}, z^{\ddagger})$ planes very near the wall ($y^* \approx 1$), for different $\bar{M}_{CLx} \in \{1.51, 2.02, 2.49\}$ at nearly constant $Re_{\tau^*} \approx 110$; also included are approximate streak boundaries (white contours $M_x = M_x|_{M'_x < 0}$) and p' -fronts (black contours $\nabla_{xz}^2 p' = 0$).

in the near-wall region ($y^* \lesssim 15$) where, at constant Re_{τ^*} , p'_{rms} increases with increasing \bar{M}_{CL_x} , especially when $\bar{M}_{CL_x} \gtrsim 2$. In contrast to the increase of the wall level $[p'_{rms}]_w^+$, the peak value $[p'_{rms}]_{PEAK}^+$ slightly decreases with \bar{M}_{CL_x} , at constant Re_{τ^*} , but the \bar{M}_{CL_x} effect on $[p'_{rms}]_{PEAK}^+$ is substantially weaker (more than threefold) than that on $[p'_{rms}]_w^+$. As a consequence, $[p'_{rms}]_w^+$, which is lower than $[p'_{rms}]_{PEAK}^+$ at incompressible and subsonic flow, increases with increasing \bar{M}_{CL_x} , to reach the peak level at $\bar{M}_{CL_x} \approx 2.3$, overcoming the peak value at higher \bar{M}_{CL_x} . The location $y_{P_{PEAK}}^*$ of the peak depends principally on \bar{M}_{CL_x} , consistently moving away from the wall with increasing \bar{M}_{CL_x} , with a much weaker dependence on Re_{τ^*} . A correlation for $[p'_{rms}]_w^+$ with respect to $(Re_{\tau^*}, \bar{M}_{CL_x}, T_r/\bar{T}_w)$, valid for airflow within the databases range, fits reasonably well both the incompressible and compressible DNS data.

Pressure–velocity correlations are strongly influenced by \bar{M}_{CL_x} in the near-wall region ($y^* \lesssim 15$), where, at constant \bar{M}_{CL_x} , they depend weakly on Re_{τ^*} . Joint p.d.f.s show that the near-wall increase of the streamwise correlation coefficient $c_{p'u'}$ is the result of increasingly intense $p' < -p'_{rms}$ events within the low-speed streaks ($u' \approx -u'_{rms}$), with little influence from the higher-speed flow region between streaks. On the other hand, the decrease of $-c_{p'v'}$ in the near-wall region appears to be the result of the global modification, with increasing \bar{M}_{CL_x} , of the flow structure both inside and between streaks. Although the importance of compressibility effects and the extent of the near-wall region where they occur depend mainly on \bar{M}_{CL_x} , there is also a weak Re_{τ^*} influence, the $Re_{\tau^*} \approx 1000$ data indicating that compressibility effects are slightly stronger at the lower Re_{τ^*} .

In contrast to these strong \bar{M}_{CL_x} effects on the near-wall p' -field, the average spanwise distance between low-speed streaks $\Lambda_S^{(z)}$ (which is a physically relevant length scale) shows little \bar{M}_{CL_x} -dependence, at constant Re_{τ^*} , when non-dimensionalised using a novel system of units introduced in the paper. This new mixed inner/outer (friction/thermodynamics) system of $(\cdot)^{\ddagger}$ units is based on $\{\bar{\tau}_w, \min_y \bar{\rho}, \max_y \bar{\mu}\}$, which in TPC flow without any artificial sink term in the energy equation are $\{\bar{\tau}_w, \rho_{CL}, \mu_{CL}\}$. This y -independent system of units corrects the geometric distortion of the rapid wall-normal variation of the $\ell_{UNIT}^*(y)$ length-unit near the wall ($y^* \lesssim 15$) and the overwhelming \bar{M}_{CL_x} -dependence of $\Lambda_S^{(z)+}$ in standard $(\cdot)^+$ wall-units which are ill-adapted for this compressible flow. Furthermore, in compressible TPC flow, these $(\cdot)^{\ddagger}$ units are almost identical to $(\cdot)^*$ HCB units for all $y^* \gtrsim 20$.

Regarding organised structures of the near-wall flow, the low-speed streaks are well identified (delimited) by the average spanwise Mach number of negative-fluctuation events, i.e. the instantaneous contours $M_x = \bar{M}_x|_{M'_x < 0}$, whereas the instantaneous contours $\nabla_{xz}^2 p' = 0$ of the in-plane Laplacian determine the fronts between $(+/-)-p'$ events. At high $\bar{M}_{CL_x} \gtrsim 2$ these p' -fronts appear organised as streamwise waves, with a bow shape between low-speed streaks, implying that they propagate faster in the high-speed region between streaks. More importantly, they extend across several streaks in the spanwise direction. When such organised p' -fronts dominate the flow field, high-intensity $(+/-)-v'$ events and p' -fronts are essentially collocated, explaining the symmetrisation of the $c_{p'v'}$ -integrand (based on the joint p.d.f.s) which reduces $-c_{p'v'}$ towards 0 with increasing \bar{M}_{CL_x} and decreasing wall distance y^* . At lower $\bar{M}_{CL_x} \lesssim 1.5$, p' -fronts no longer exhibit

this wave-packet-like structure, except for some relatively rare instances, but become elongated structures mostly aligned with the streaks which are no longer collocated with high-intensity $(+/-) - v'$ events.

Further research is required to identify the precise dynamics of these organised pressure waves, their interaction with the wall-normal vorticity ω'_y structures which create the near-wall low-speed streaks, and their origin in a spanwise array of $(+/-) - \bar{M}_x$ mixing layers embedded in a strongly stratified mean flow, as well as the effect of the wall echo on p' in this very-near-wall region. Obviously the near-wall compressibility effects are induced by a combination of mean-flow stratification (Morkovin 1962) and compressible turbulence (fluctuating dilatation and fluctuating density). Specific source terms $(-\rho D_t \Theta - D_t V \cdot \text{grad } \rho)'$ are included in the Poisson equation for $\nabla^2 p'$ (Gerolymos *et al.* 2013, (A1c), pp. 45–46), and the Green's function solution for the corresponding contributions to p' could contribute to assess the relative importance of each mechanism. Another, single-point-statistics approach, is provided by appropriate rewriting of the heat-conduction term $\overline{p' \partial_{x_\ell} q'_\ell}$ in the transport equation for $\overline{p'^2}$ (Gerolymos & Vallet 2014, (4.11a), p. 740) to reveal the $\text{grad}(1/\rho)$ terms hidden in $\partial_{x_\ell} T'$, accounting explicitly for stratification effects. Both these complementary approaches are the subject of ongoing research.

Funding. The computations reported in the present work were performed using HPC resources allocated at PRACE-JUWELS (project 2021-240083) GENCI-IDRIS/TGCC/CINES (grants 2010-022139 to 2021-022139) and at ICS-UPMC (ANR-10-EQPX-29-01).

Declaration of interests. The authors report no conflict of interest.

Data availability statement. Data will be made available at http://www.aerodynamics.fr/DNS_database/.

Author ORCIDs.

 G.A. Gerolymos <https://orcid.org/0000-0003-3207-5659>;

 I. Vallet <https://orcid.org/0000-0003-1286-831X>.

Author contributions. The authors are listed alphabetically and have both contributed equally to the entire work reported in the paper, and to writing the paper.

REFERENCES

- ADRIAN, R.J. 2007 Hairpin vortex organization in wall turbulence. *Phys. Fluids* **19**, 041301.
- DEL ÁLAMO, J.C. & JIMÉNEZ, J. 2009 Estimation of turbulent convection velocities and corrections to Taylor's approximation. *J. Fluid Mech.* **640**, 5–26.
- BAE, H.J. & LEE, M. 2021 Life cycle of streaks in the buffer layer of wall-bounded turbulence. *Phys. Rev. Fluids* **6**, 064603.
- BATCHELOR, G.K. 1967 *An Introduction to Fluid Dynamics*. Cambridge University Press.
- BERNARD, P.S. 2019 On the inherent bias of swirling strength in defining vortical structure. *Phys. Fluids* **31**, 035107.
- BERNARDINI, M. & PIROZZOLI, S. 2011 Wall pressure fluctuations beneath supersonic turbulent boundary-layers. *Phys. Fluids* **23**, 085102.
- BOWERSOX, R.D.W. 2009 Extension of equilibrium turbulent heat flux models to high-speed shear flows. *J. Fluid Mech.* **633**, 61–70.
- BRADSHAW, P. 1977 Compressible turbulent shear layers. *Annu. Rev. Fluid Mech.* **9**, 33–54.
- CHEN, X. & SREENIVASAN, K.R. 2022 Law of bounded dissipation and its consequences in turbulent wall flows. *J. Fluid Mech.* **933**, A20.
- CHERNYSHENKO, S.I. & BAIG, M.F. 2005a The mechanism of streak formation in near-wall turbulence. *J. Fluid Mech.* **544**, 99–131.
- CHERNYSHENKO, S.I. & BAIG, M.F. 2005b Streaks and vortices in near-wall turbulence. *Phil. Trans. R. Soc. Lond. A* **363**, 1097–1107.

- CHU, B.T. & KOVÁSZNAY, L.S.G. 1958 Nonlinear interactions in a viscous heat-conducting compressible gas. *J. Fluid Mech.* **3**, 494–514.
- COLEMAN, G.N., KIM, J. & MOSER, R.D. 1995 A numerical study of turbulent supersonic isothermal-wall channel flow. *J. Fluid Mech.* **305**, 159–183.
- VAN DRIEST, E.R. 1951 Turbulent boundary-layer in compressible fluids. *J. Aerosp. Sci.* **18** (3), 145–160.
- FOYSI, H., SARKAR, S. & FRIEDRICH, R. 2004 Compressibility effects and turbulence scalings in supersonic channel flow. *J. Fluid Mech.* **509**, 207–216.
- GEROLYMOS, G.A., SÉNÉCHAL, D. & VALLET, I. 2009 Very-high-order WENO schemes. *J. Comput. Phys.* **228**, 8481–8524.
- GEROLYMOS, G.A., SÉNÉCHAL, D. & VALLET, I. 2010 Performance of very-high-order upwind schemes for dns of compressible wall-turbulence. *Intl J. Numer. Meth. Fluids* **63**, 769–810.
- GEROLYMOS, G.A., SÉNÉCHAL, D. & VALLET, I. 2013 Wall effects on pressure fluctuations in turbulent channel flow. *J. Fluid Mech.* **720**, 15–65.
- GEROLYMOS, G.A. & VALLET, I. 2014 Pressure, density, temperature and entropy fluctuations in compressible turbulent plane channel flow. *J. Fluid Mech.* **757**, 701–746.
- GEROLYMOS, G.A. & VALLET, I. 2016 The dissipation tensor ε_{ij} in wall turbulence. *J. Fluid Mech.* **807**, 386–418.
- GEROLYMOS, G.A. & VALLET, I. 2018 Correlation coefficients of thermodynamic fluctuations in compressible aerodynamic turbulence. *J. Fluid Mech.* **851**, 447–478.
- GEROLYMOS, G.A. & VALLET, I. 2019 Destruction-of-dissipation and time-scales in wall turbulence. *Phys. Fluids* **31** (5), 055103.
- HOYAS, S. & JIMÉNEZ, J. 2006 Scaling of the velocity fluctuations in turbulent channels up to $Re_\tau = 2003$. *Phys. Fluids* **18**, 011702.
- HOYAS, S., OBERLACK, M., ALCÁNTARA-ÁVILA, F., KRAHEBERGER, S. & LAUX, J. 2022 Wall turbulence at high friction Reynolds numbers. *Phys. Rev. Fluids* **7**, 014602.
- HU, Z.W. & SANDHAM, N.D. 2001 DNS databases for turbulent Couette and Poiseuille flow. *Tech. Rep.* AFM–01–04. AFM Research Group, School of Engineering Sciences, University of Southampton.
- HUANG, P.G., COLEMAN, G.N. & BRADSHAW, P. 1995 Compressible turbulent channel flows: DNS results and modelling. *J. Fluid Mech.* **305**, 185–218.
- KIM, J. 1989 On the structure of pressure fluctuations in simulated turbulent channel-flow. *J. Fluid Mech.* **205**, 421–451.
- KIM, J. & HUSSAIN, F. 1993 Propagation velocity of perturbations in turbulent channel flow. *Phys. Fluids A* **5** (3), 695–706.
- KIM, J., MOIN, P. & MOSER, R. 1987 Turbulence statistics in fully developed channel flow at low-Reynolds-number. *J. Fluid Mech.* **177**, 133–166.
- KLEWICKI, J.C., PRIYADARSHANA, P.J.A. & METZGER, M.M. 2008 Statistical structure of the fluctuating wall pressure and its in-plane gradients at high Reynolds number. *J. Fluid Mech.* **608**, 195–220.
- LEE, M. & MOSER, R.D. 2015 DNS of turbulent channel flow up to $Re_\tau \approx 5200$. *J. Fluid Mech.* **774**, 395–415.
- LIEPMANN, H.W. & ROSHKO, A. 1957 *Elements of Gasdynamics*. John Wiley and Sons.
- MODESTI, D. & PIROZZOLI, S. 2016 Reynolds and Mach number effects in compressible turbulent channel. *Intl J. Heat Fluid Flow* **59**, 33–49.
- MONKEWITZ, P.A. 2022 Asymptotics of streamwise Reynolds stress in wall turbulence. *J. Fluid Mech.* **931**, A18.
- MORKOVIN, M.V. 1962 Effects of compressibility on turbulent flows. In *Proceedings of the International Colloquium on Mechanics of Turbulence, Marseille* (ed. A. Favre), Colloques Internationaux du CNRS, vol. 108, pp. 367–380. Editions du CNRS.
- MOSER, R.D., KIM, J. & MANSOUR, N.N. 1999 Direct numerical simulation of turbulent channel flow up to $Re_\tau = 590$. *Phys. Fluids* **11** (4), 943–945.
- PANTANO, C. & SARKAR, S. 2002 A study of compressibility effects in the high-speed turbulent shear layer using direct simulation. *J. Fluid Mech.* **451**, 329–371.
- PANTON, R.L. 2001 Overview of self-sustaining mechanisms of wall turbulence. *Prog. Aerosp. Sci.* **37**, 341–383.
- PANTON, R.L., LEE, M. & MOSER, R.D. 2017 Correlation of pressure fluctuations in turbulent wall layers. *Phys. Rev. Fluids* **2**, 094604.
- PANTON, R.L. & LINEBARGER, J.H. 1974 Wall pressure spectra calculations for equilibrium boundary-layers. *J. Fluid Mech.* **65**, 261–287.
- PAPAMOSCHOU, D. & ROSHKO, A. 1988 The compressible turbulent shear layer: an experimental study. *J. Fluid Mech.* **197**, 453–477.

Pressure fluctuations in compressible wall turbulence

- SARKAR, S. 1992 The pressure-dilatation correlation in compressible flows. *Phys. Fluids A* **4** (12), 2674–2682.
- SCHLATTER, P., LI, Q., BRETHOUWER, G., JOHANSSON, A.V. & HENNINGSON, D.S. 2010 Simulations of spatially evolving turbulent boundary-layers up to $Re_\theta = 4300$. *Intl J. Heat Fluid Flow* **31**, 251–261.
- SMITS, A.J. & DUSSAUGE, J.P. 2006 *Turbulent Shear Layers in Supersonic Flow*. Springer.
- TANG, J., ZHAO, Z., WAN, Z.H. & LIU, N.S. 2020 On the near-wall structures and statistics of fluctuating pressure in compressible turbulent channel flows. *Phys. Fluids* **32**, 115121.
- TRETTEL, A. & LARSSON, J. 2016 Mean velocity scaling for compressible wall turbulence with heat transfer. *Phys. Fluids* **28**, 026102.
- TRITTON, D.J. 1988 *Physical Fluid Dynamics*. Oxford University Press.
- TSUJI, Y., FRANSSON, J.H.M., ALFREDSSON, P.H. & JOHANSSON, A.V. 2007 Pressure statistics and their scalings in high-Reynolds-number turbulent boundary-layers. *J. Fluid Mech.* **585**, 1–40.
- TSUJI, Y., IMAYAMA, S., SCHLATTER, P., ALFREDSSON, P.H., JOHANSSON, A.V., HUTCHINS, N. & MONTY, J. 2012 Pressure fluctuation in high-Reynolds-number turbulent boundary-layer: results from experiments and DNS. *J. Turbul.* **13**, 000050.
- VREMAN, A.W. & KUERTEN, J.G.M. 2014 Statistics of spatial derivatives of velocity and pressure in turbulent channel flow. *Phys. Fluids* **26**, 085103.
- WANG, W., PAN, C. & WANG, J. 2019 Wall-normal variation of spanwise streak spacing in turbulent boundary-layer with low-to-moderate Reynolds number. *Entropy* **21** (1), 24.
- YU, M. & XU, C.X. 2021 Compressibility effects on hypersonic turbulent channel flow with cold walls. *Phys. Fluids* **33**, 075106.
- YU, M., XU, C.X. & PIROZZOLI, S. 2019 Genuine compressibility effects in wall-bounded turbulence. *Phys. Rev. Fluids* **4**, 123402.
- YU, M., XU, C.X. & PIROZZOLI, S. 2020 Compressibility effects on pressure fluctuations in compressible turbulent channel flows. *Phys. Rev. Fluids* **5**, 113401.
- ZHANG, C., DUAN, L. & CHOUDHARI, M.M. 2017 Effect of wall cooling on boundary-layer-induced pressure fluctuations at Mach 6. *J. Fluid Mech.* **822**, 5–30.